# DYNAMICS AND RHEOLOGY OF CONCENTRATED SUSPENSIONS OF RIGID FIBERS

By

SAIF SHAIKH

A DISSERTATION PRESENTED TO THE GRADUATE SCHOOL
OF THE UNIVERSITY OF FLORIDA IN PARTIAL FULFILLMENT
OF THE REQUIREMENTS FOR THE DEGREE OF
DOCTOR OF PHILOSOPHY

UNIVERSITY OF FLORIDA

2017

To my family, you are the pillars upon which I stand tall

ACKNOWLEDGMENTS

The work presented in this dissertation is in partial fulfillment of a dual-degree program between the College of Engineering at the University of Florida and Aix-Marseille Université, Marseille, France. I am grateful to the institutions and funding sources that have facilitated this project and collaboration.

To begin, I am indebted to my doctoral advisors, Dr. Jason E. Butler and Dr. Élisabeth Guazzelli who have greatly supported me through this program. Dr. Butler has ingrained the critical thinking and problem solving skills required to excel as a researcher and a thinker. Through Dr. Guazzelli's vast experience, I have developed a steady hand and a keen mind; skills that have made me a competent experimental scientist along with granting me the freedom to understand that failure is an integral part of the scientific process. Together, they have taught me to never settle for anything less than the best version of my work. My present and future successes are because of the time and effort they have put into my project and me.

I would also like to thank my French and American committees. Dr. Ranga Narayanan at the University of Florida continually provided insight into my project, and always reminded me to take a step back from the details to ask bigger questions. His advice has been instrumental in helping me adhere to the large scale contributions of this project. Dr. Renwei Mei and Dr. Anuj Chauhan must also be thanked for keeping an eye on the smaller details and for helping me approach issues from a different perspective. Special mention must be made of Dr. Elisabeth Lemaire and Dr. Anke Lindner for agreeing to be reporters for my dissertation.

My scientific journey would not be complete without the many hours spent learning about relevant concepts from Dr. Olivier Pouliquen, Dr. Bloen Metzger, and Dr. Henri Lhussier at Aix-Marseille Université. Their systematic instruction has deepened my understanding of my project in particular and my field as a whole.

Immense thanks must be given in particular to Scott Strednak from UF and Franco Tapia from AMU. Franco was instrumental in assisting with the experiments using pressure-imposed rheometer and with helping me with data analyses. In a similar vein, Scott has been indispensable with his assistance with running the shear-induced migration experiments and his lion's share in the subsequent analyses. I have learned a lot by working alongside them and hope to repay them in kind in the near future.

My experience in France would be an entirely lonesome and dreary experience without the various people who made it a life-changing one. Firstly, I must effusively thank Dr. Laurence Bergougnoux who tirelessly held my hand while navigating the French language, bureaucracy, and culture as a whole. Mathieu Souzy and his wife Sandra have been extremely patient with my negligible french and have provided me with many french lessons over the years. Any success I had in grasping their language is attributed in large part to them. My french colleagues, both past and present, Joris Chateau, Cecile Clavaud, Antoine Berut, Jean-François Louf, and others have become life-long friends even though they are continents away.

Back in Gainesville, my labmates Ryan Montes, Mert Arca, Phong Pham, and Braden Snook have served as constant inspiration for me. Our talks, both scientific and casual have made me a better scientist and a more wholesome person. This space is not enough to mention everyone who has helped through the years of this program but I hope they are aware of my gratitude.

To Deborah Spiess, thank you for being by my side through this journey and for being a constant bastion on whom I could always depend. You have made my graduate program a truly happy experience. To my family, your constant support and guidance has not been overlooked. I would like to thank my father, Asif Shaikh, who taught me to always strive for excellence in whatever I do. Thank you to my mother, Zarin who has forever instilled in me a sense of determination tempered with empathy, and my brother, Mikail Shaikh, who was always there for me. I hope to make you proud.

TABLE OF CONTENTS

LIST OF TABLES

LIST OF FIGURES

Abstract of Dissertation Presented to the Graduate School
of the University of Florida in Partial Fulfillment of the
Requirements for the Degree of Doctor of Philosophy

DYNAMICS AND RHEOLOGY OF CONCENTRATED SUSPENSIONS OF RIGID FIBERS

By

Saif Shaikh

December 2017

Chair: Jason E. Butler
Major: Chemical Engineering

A combined work of experiments and data analyses is proposed to investigate the dynamics and rheology of highly concentrated suspensions of non-colloidal rigid rods in a Newtonian fluid. Detailed measurements of the rheology and the microstructure are made using a variety of experimental devices with different geometries and imposed flows. Standard rheology experiments (volume-controlled rheology), as well as a novel method of rheometry, are carried out to measure torques, particle pressures, and volume fractions at high concentration (pressure-controlled rheology). Another experiment has been designed and constructed to study the microstructure (spatial and orientation distribution) of a suspension of rigid rods in an oscillatory parabolic flow. Though the flow is reversible in these systems, the changes in the microstructure are irreversibile in the case of concentrated suspensions due to particle interactions. The microstructure is affected by, and has an effect, on the imposed flows; this non-linear dependency includes hydrodynamic interactions. The purpose of these experiments is to gain insight into phenomena such as apparent shear-thinning at high shear rates and demixing due to shear-induced migration.

# CHAPTER 1
# INTRODUCTION

Suspensions are a class of complex fluid in which insoluble particles, either solid or liquid, are dispersed in a liquid phase [1]. Highly concentrated particle-liquid suspensions are ubiquitous in nature and in industry. In nature, lava and silt-laden rivers are macroscale examples of suspensions. At smaller scales, blood is an example of a suspension where disc-like platelets are suspended in plasma. Elongated particles can be found in wide variety of applications. For example, they are added to concrete slurries to reinforce its strength and enhance its performance [2], rheological properties of drilling fluids are altered by the addition of rod-like particles [3, 4], and the production of paper from wood fibers is an important application of non-spherical particle suspensions. From pharmaceuticals to oil refineries, paper-mills, manufacturing, and waste disposal, the industrial manifestations and applications of suspensions are commonplace.

From an engineering standpoint, better predictions of the dynamics of particle suspensions help in designing pumps, piping, mixers, and other flow and process equipment, with the goal of optimizing performance and energy consumption while also reducing the capital and operating costs. As a starting point, rheological properties of suspensions are needed as an input for even the most basic models of their macroscopic flow, and modern rheometers have made it possible to quickly generate a large amount of data once samples have been prepared. Yet, accurately interpreting and successfully utilizing the data from rheometers remains a significant problem for a wide class of suspensions.

As an example of the difficulties, consider the evaluation of the shear rheology of non-colloidal spheres suspended in a Newtonian fluid, where the density of the fluid

---

**Author's note:** This dissertation is in partial fulfillment of a dual-degree doctoral program between the College of Engineering at the University of Florida, Gainesville, FL. USA and Aix-Marseille Université, Marseille, France.

matches the density of the particles. As summarized in his Bingham award lecture, Acrivos [5] found large discrepancies reported in the literature for the viscosity at high values of the particle concentration. At least one clear issue was identified as a source for the discrepencies: for a suspension under shear in a Couette geometry, the particles were found to migrate over long times from the gap between the shearing surfaces to the region below the bob where the shear rate vanishes [6]. As a result of the migration, the concentration in the gap is lower than the bulk, and the torque required to rotate the shearing surfaces at a fixed rate drops. The viscosity consequently appears to be lower than it should, and the value that is measured will depend on both the time of the measurement and the specific dimensions of the geometry used. Even at short times, the viscosity appears to increase due to migration across the gap of the Couette cell [6]. The migration is driven by the non-uniformity of the shear gradient and its coupling with the shear-induced diffusion of the particles [7, 8], according to one theory, and normal stresses [9] in the suspensions, according to another. Consequently, rheological measurements of this class of suspension must be interpreted with care, as unavoidable shear-gradients may cause an inhomogeneous distribution of particles and erroneous values of the viscosity as a function of concentration.

Similarly, characterizing the rheology of elongated particles, such as rigid fibers which are non-colloidal and neutrally buoyant, presents a range of challenges. Little work has been done examining the shear-induced migration of rigid fibers in flows, though experiments by Mondy *et al.* [10] have verified that migration occurs in Couette cells at sufficiently high concentrations. For suspensions of rods, additional complexities arise due to the interaction of the rods with the boundaries. For example, Figure 1-1 shows measurements of the normal stress differences for rod suspensions at concentrations of $n > 1/L^2 d$, where $n$ is the number density and the length and diameter of the rod are $L$ and $d$ respectively. The normal stress differences measured from free surface flows by Snook *et al.* [11] were performed in shearing flows where the bounding

wall separation, $H$, was much greater than the particle length. Measurements in more confined geometries using traditional rheological equipment, also shown in Figure 1-1, give results that can be different by large factors. Results from simulations [11], which agree at least qualitatively with the measurements, reveal that the differences are due directly to the microstructure: the bounding walls prevent particles from rotating and moving freely, altering the structure and, consequently, the rheology. The disturbance in the structure imposed by the wall propagates into the fluid for a distance much larger than expected, and the measured rheology will be that of the bulk material only for very large values of $H/L$.

This dissertation presents results from investigations of the dynamics and rheology of non-colloidal suspensions of rigid rods. Multiple constraints were placed on both the fluid and particle properties in the work discussed here. In addition to having an aspect ratio $A = L/d$ much larger than one, the fibers (or rods) are straight and rigid. The particles of interest are large, so hydrodynamic forces are dominant and Brownian fluctuations safely can be assumed to have no impact on the dynamics and rheology of the suspensions. All of the fibers in a suspension are identical (monodisperse) with regard to their size and shape, and the effects of gravity are removed by matching the fluid density to the density of the particles. The suspending fluid itself is Newtonian and sufficiently viscous so that inertia is negligible.

The investigations were aimed at addressing questions introduced above, regarding the proper characterization and interpretation of the rheology when the concentration is high and phenomena such as boundary effects and shear-induced migration become relevant. Before introducing the specific investigations that were performed in subsections 1.3.1 and 1.3.2, the following sections briefly review the motion of a rod in dilute suspensions and then the physical mechanisms that influence the motion of rods in suspension at higher concentrations.

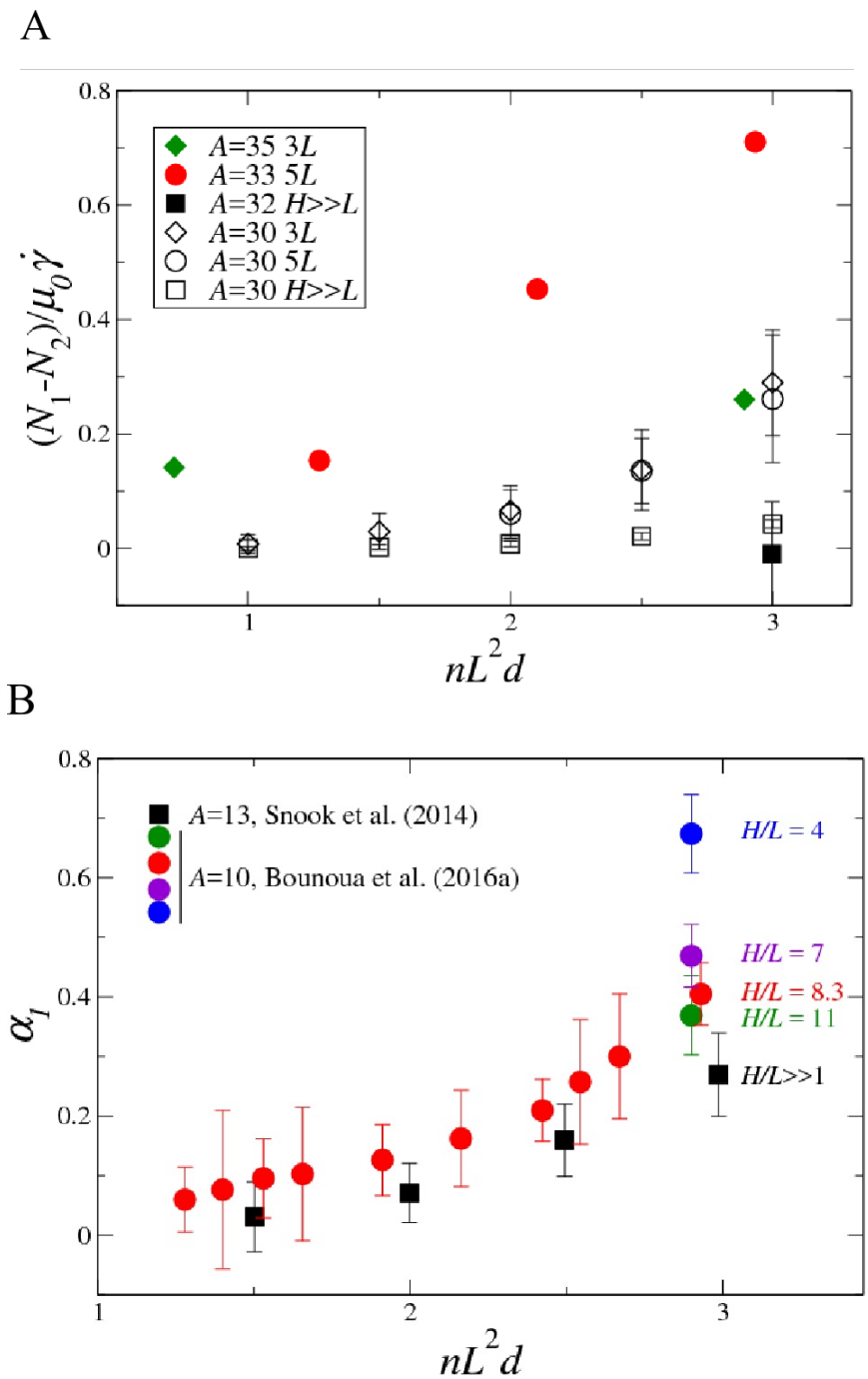


Figure 1-1. Measurements and predictions of the normal stress differences $N_1$ and $N_2$ in suspensions of rigid fibers over a range of aspect ratios $A$ and confinements, $H$. A) The value of $N_1 - N_2$, normalized by the stress $\mu_o\dot{\gamma}$ of the suspending fluid of viscosity $\mu_0$ sheared at a rate of $\dot{\gamma}$, is shown from simulations [11] (open symbols) and experiments (solid symbols) of Keshtkar *et al.* [12] (green), Bounoua *et al.* [13] (red), and Snook *et al.* [11] (black) for different levels of confinement $H$. B) Experimental measurements of the first normal stress coefficient $\alpha_1 = N_1/(\mu\dot{\gamma})$ for fibers of low aspect ratio over a range of concentrations and confinements.

## 1.1 One Fiber in Flow

The center of mass $\boldsymbol{x}_\alpha$ of a rigid fiber $\alpha$ that is force-free moves with the flow field as evaluated at its center as

$$\dot{\boldsymbol{x}}_\alpha = \boldsymbol{u}(\boldsymbol{x}_\alpha), \tag{1–1}$$

where $\dot{\boldsymbol{x}}_\alpha$ is the center of mass motion for imposed flow fields $\boldsymbol{u}(\boldsymbol{x}_\alpha)$ that are linear and where the particle is far from boundaries. Additional corrections to the flow field must be included for non-linear flows and to account for bounding walls,

$$\dot{\boldsymbol{x}}_\alpha = \frac{1}{L}\int_{-L/2}^{L/2} \boldsymbol{u}\left(\boldsymbol{x}_\alpha + s_\alpha \boldsymbol{p}_\alpha\right) ds_\alpha, \tag{1–2}$$

where $\boldsymbol{u}$ is the sum of the imposed flow and any additional velocity disturbances in the fluid, $\boldsymbol{p}_\alpha$ is the unit vector along the fiber major axis, and $s_\alpha$ is the position along that axis. For instance, the flow field for a parabolic flow between two parallel walls separated by distance $2H$, with maximum velocity $U_m$ at the center between the walls is,

$$\boldsymbol{u} = \frac{U_m}{H^2}(H^2 - y^2)\boldsymbol{\delta}_x, \tag{1–3}$$

where $y$ is the co-ordinate in the gradient direction measured from the mid-plane between the walls, and $\boldsymbol{\delta}_x$ is the direction of the flow. The resultant motion of the rod can be calculated from Equation 1–2,

$$\dot{\boldsymbol{x}}_\alpha = \frac{U_m}{H^2}(H^2 - (\boldsymbol{x}_\alpha \cdot \boldsymbol{\delta}_y)^2)\boldsymbol{\delta}_x - \frac{U_m L^2}{12H^2}(\boldsymbol{p}_\alpha \cdot \boldsymbol{\delta}_y)\boldsymbol{\delta}_x, \tag{1–4}$$

where $(\boldsymbol{x}_\alpha \cdot \boldsymbol{\delta}_y)$ is the center-of-mass coordinate of the rod $\alpha$ in the gradient direction $\boldsymbol{\delta}_y$. The first term is the motion of the rod corresponding to the velocity of the fluid evaluated at the center of the rod, and the second term corresponds to the correction to the rod velocity due to the curvature of the flow field. In equation 1–4, the effects of the bounding wall on the center-of-mass motion have been ignored, though methods exist for incorporating those effects have been developed [14, 15]. As originally shown by Ganatos *et al.* [16], a single rod can migrate across streamlines, with the rate and

direction of the migration depending on the orientation. This is very different from a single sphere in a simple shear flow near a bounding wall, which simply translates parallel to the wall without crossing stream lines.

To calculate the velocities of a particle, whether in the case of Equation 1–4 or any other motion, the orientation is generally needed and can be calculated from an initial condition and velocity. For an isolated ellipsoid in a shearing flow, the ellipsoid rotates with an orientation velocity first described by Jeffery [17] as

$$\dot{\boldsymbol{p}}_\alpha = \boldsymbol{\Omega} \cdot \boldsymbol{p}_\alpha + \frac{A^2 - 1}{A^2 + 1} \left( \boldsymbol{I} - \boldsymbol{p}_\alpha \boldsymbol{p}_\alpha \right) \cdot \boldsymbol{E} \cdot \boldsymbol{p}_\alpha. \tag{1–5}$$

The Jeffery orbit, as derived from this equation, is a family of closed rotations that depend on the initial orientation of the rod. The orbit can be defined by an orbit constant,

$$C = \frac{1}{A} \tan(\theta_z) \left( A^2 \cos^2(\phi_y) + \sin^2(\phi_y) \right)^{1/2}, \tag{1–6}$$

where the angles $\theta_z$ and $\phi_y$ are specified in Figure 1-2. According to Equation 1–5, the rod simply rotates with the rate of rotation, $\boldsymbol{\Omega} = \frac{1}{2}[(\nabla \boldsymbol{u} - \nabla \boldsymbol{u})^T]$, and a fraction of the rate of extension, $\boldsymbol{E} = \frac{1}{2}[(\nabla \boldsymbol{u} + \nabla \boldsymbol{u})^T]$. Figure 1-2 shows the rotational motion of an ellipsoid in a simple shear flow, $\boldsymbol{u} = \dot{\gamma} y \boldsymbol{\delta}_x$, where the aspect ratio $A$ of the ellipsoid was set to 10. Equation 1–5 is not limited to just ellipsoids, as originally derived by Jeffery [17]. By replacing $A$ with an effective aspect ratio ($A_e$), elongated particles with a large range of specific shapes can be calculated. For example, Bretherton [18] showed that setting $A_e = 0.8A$ gives an accurate calculation for the rotational dynamics a cylindrical rod, and was later confirmed my Mason *et al.* [19, 20].

Though all of the work reported in this dissertation regards fibers that are neutrally buoyant, in suspensions at high concentration inter-particle contact forces can be present. Hence, it is instructive to consider the motion of an isolated rod in a quiescent fluid, which differs qualitatively from that of a sphere. Here, the center of mass motion

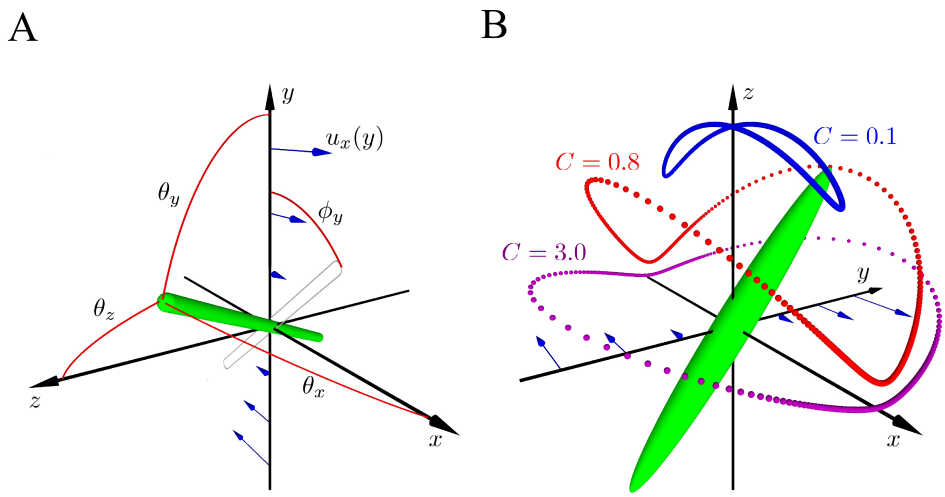


Figure 1-2. A rigid fiber in a shear flow. A) The shear flow $\dot{\boldsymbol{x}}_\alpha = \dot{\gamma}(\boldsymbol{x}_\alpha \cdot \boldsymbol{\delta}_y)\boldsymbol{\delta}_x$, is shown, where $\theta_z$ is the angle of the fiber with the vorticity axis and $\phi_y$ is the angle between the gradient axis $y$ and the projection (gray outline) of the fiber onto the flow-gradient $(x - y)$ plane. B) Jeffery orbits for three initial conditions ($C = 0.1$, 0.8, and 3.0) are shown for an ellipsoid of aspect ratio $A = 10$. The ellipsoid rotates fastest when aligned in the gradient-vorticity plane ($\theta_x = \pm\pi/2$) and rotation slows when the orientation is near the flow-vorticity plane; the relative rate of rotation is indicated by the spacing of the points which are plotted at equivalent intervals in time.

$\dot{\boldsymbol{x}}_\alpha$ is due to a force, $\boldsymbol{F}_\alpha$, and is given by

$$\dot{\boldsymbol{x}}_\alpha = \frac{ln(2A)}{4\pi\eta_f L}(\boldsymbol{I} + \boldsymbol{p}_\alpha\boldsymbol{p}_\alpha) \cdot \boldsymbol{F}_\alpha, \tag{1–7}$$

where the fluid viscosity is $\eta_f$. This is the leading-order result predicted by slender body theory [21, 22]. The dependence of the motion of the rod on the orientation is clearly seen by looking at the velocity of the rod when it is parallel to the force, $U_\parallel = 2F_\alpha ln(2A)/4\pi\eta_f L$, versus the motion when the rod is oriented perpendicular to the force, $U_\perp = U_\parallel/2$. Also for rods oriented at at angle with the direction of the applied force, components of motion exist in the direction perpendicular to the force. For spheres, the motion is always in the same direction of the force for zero Reynolds number conditions.

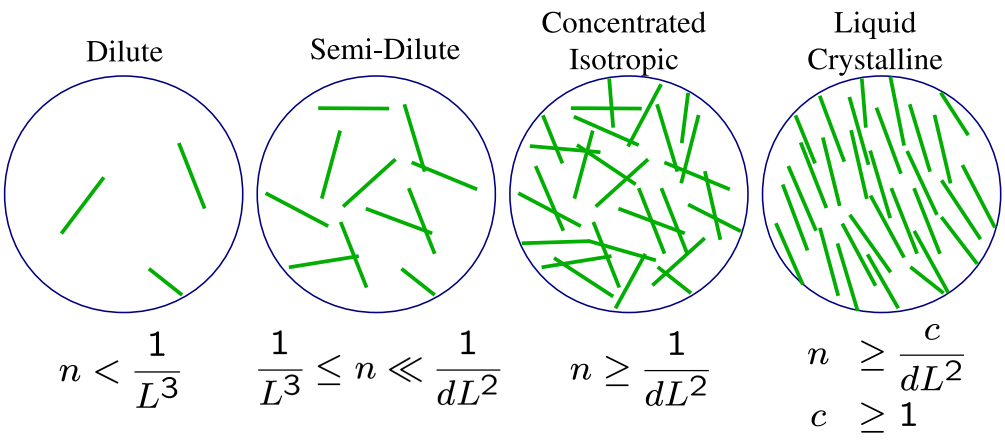


Figure 1-3. Regimes of concentrations of suspensions of rigid rods as suggested by Doi and Edwards. In the concentrated regime, $nL^2d \geq 1$, contacts between rods become significant. At values of $nL^2d \approx c > 1$, the rods must align in order to fit within the specified volume. At these concentrations, the rods "crystallize" into a highly ordered state.

## 1.2 Suspensions with Interactions

As the concentration in a suspension increases beyond dilute, interactions between particles begin to significantly impact the dynamics. Regimes of concentrations for suspensions of rods, as defined by Doi and Edwards [23], are shown in Figure 1-3 in terms of the number density of the suspension $n = N/V$, where $N$ is the number of fibers and $V$ is the total volume of the suspension. Concentrated suspensions are those for which $nL^2d \geq 1$; here, $L$ is the length of the rod and $d$ is its diameter. At $nL^2d \geq 1$, the free rotation of any rod is hindered by surrounding rods, giving rise to rod-rod contacts that substantially influence the dynamics and microstructure of the suspension. These changes in microstructure affect the macroscopic measurements of the suspension, such as viscosity.

Even widely separated particles can be affected by each other. When a force is applied to a particle within a viscous fluid, there is a disturbance in the fluid velocity in response to the force. These disturbances affect the motion of other particles in the fluid, giving rise to non-linear dependencies that are known as "hydrodynamic interactions". To model multi-body hydrodynamic interactions, the most straightforward

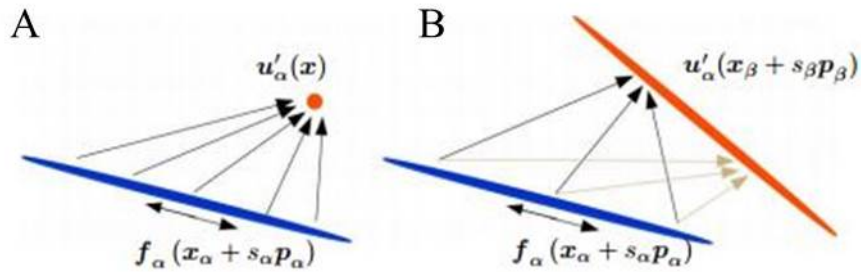


Figure 1-4. Schematic of the velocity disturbance caused by a single rod $\alpha$ on a point $\boldsymbol{x}$. A) The velocity disturbance caused by a rod $\alpha$ can be calculated at any point $\boldsymbol{x}$ by integrating the Greens function and line force density over the length of the rod and indicated in Equation 1–8. B) To calculate the motion of a rod $\beta$ in the presence of the rod $\alpha$, the velocity disturbance caused by rod $\alpha$ can be evaluated at every point along the centerline of $\beta$ and then integrated to give the motion.

case is to first consider the influence of the forces of one fiber on another as illustrated in Figure 1-4(a). Using the slender body hypothesis [21], i.e, for a very high aspect ratio, the rod can be approximated by a line of point forces, and the disturbance velocity, $\boldsymbol{u}'_\alpha(\boldsymbol{x})$, due to any rod $\alpha$, calculated at any point, $\boldsymbol{x}$ can be calculated from

$$\boldsymbol{u}'_\alpha(\boldsymbol{x}) = \int_{-L/2}^{L/2} \boldsymbol{G}(\boldsymbol{x}, \boldsymbol{x}_\alpha + s_\alpha \boldsymbol{p}_\alpha) \cdot \boldsymbol{f}(\boldsymbol{x}_\alpha + s_\alpha \boldsymbol{p}_\alpha) ds_\alpha, \tag{1–8}$$

which is the summation (integration) of the disturbances created by each point over the entire length of the fiber. Here, $\boldsymbol{G}(\boldsymbol{x}, \boldsymbol{x}_\alpha + s_\alpha \boldsymbol{p}_\alpha)$ is the Greens function for Stokes flow evaluated at any point at a distance $s_\alpha$ along the axis of the fiber. The line force density is given by $\boldsymbol{f}(\boldsymbol{x}_\alpha + s_\alpha \boldsymbol{p}_\alpha)$. Here, the Greens function $\boldsymbol{G}(\boldsymbol{x}, \boldsymbol{x}_\alpha + s_\alpha \boldsymbol{p}_\alpha)$ is given by

$$\boldsymbol{G}(\boldsymbol{x}, \boldsymbol{x}_\alpha + s_\alpha \boldsymbol{p}_\alpha) = \frac{1}{8\pi\eta}\left(\frac{\boldsymbol{I}}{r} - \frac{\boldsymbol{r}\boldsymbol{r}}{r^3}\right), \tag{1–9}$$

where $\boldsymbol{I}$ is the identity matrix, $\boldsymbol{r} = (\boldsymbol{x}_\alpha + s_\alpha \boldsymbol{p}_\alpha) - \boldsymbol{x}$, and $r = |\boldsymbol{r}|$.

Furthermore as illustrated in Figure 1-4(b), the disturbance velocity can be calculated at any point on another fiber $\beta$ from Equation 1–8 and the resulting motion of fiber

$\alpha$ calculated from Equation 1–2,

$$\dot{\boldsymbol{x}}_\beta = \frac{1}{L}\int_{-L/2}^{L/2}\int_{-L/2}^{L/2} \boldsymbol{G}(\boldsymbol{x}_\beta + s_\beta \boldsymbol{p}_\beta, \boldsymbol{x}_\alpha + s_\alpha \boldsymbol{p}_\alpha)\cdot \boldsymbol{f}(\boldsymbol{x}_\alpha + s_\alpha \boldsymbol{p}_\alpha) ds_\alpha ds_\beta, \tag{1–10}$$

where $s_\beta$ is a position along the rod $\beta$.

Consider the motion of only three rods, each acted upon by a force: the disturbance generated by the force on each rod results in a disturbance on the other two. The presence of the disturbance on any one rod due to the other two alters the force distribution, and this alteration of the force distribution must be considered when calculating the disturbance velocity. This cycle of reflecting the velocity disturbances and force distributions continues endlessly and would appear to be insolvable. Consequently, simulating the collective dynamics of the rods requires an approximation, and a very convenient one is available. Each reflection of an interaction is significantly weaker than the previous, by a factor of

$$\frac{1}{\ln(2A)}\frac{L}{r}, \tag{1–11}$$

where $r$ is a measure of the separation distance between the rods [24]. For the $M^{th}$ reflection, the change to the motion of a rod would be

$$\left(\frac{1}{\ln(2A)}\frac{L}{r}\right)^M. \tag{1–12}$$

For widely spaced rods of high aspect ratio, the error in truncating the interactions after $M = 2$ or $3$ is small. Such an approach is commonly used when simulating the collective motion of spheres where the reflections are stronger. For spheres of radius $a$, each reflection $M$ of the interactions contributes a velocity that scales as a fraction,

$$\left(\frac{a}{r}\right)^M, \tag{1–13}$$

of the leading contribution to the velocity [25].

Note that the rapid decay of the interactions given by Equation 1–11 is the basis of the frequent claim that hydrodynamic interactions can be ignored in suspensions of

slender bodies. While true for relatively dilute suspensions (i.e. $L/r$ small) for rods as the aspect ratio goes to infinity, the approximation must be used with caution. Even in this limit of dilute concentrations, fluctuations in the concentration that generate pairs of nearby rods can make the approximation invalid [26, 27].

Although hydrodynamic interactions are crucial to studies in the semi-dilute regime, studies in the denser regime of suspensions claim that long-range hydrodynamics, and even short range lubrication interactions, are not necessary to capture the dynamics and rheology of fiber systems. One of the primary aims of this work is to test this idea.

### 1.3 Moving Toward Concentrated Suspensions

At higher concentrations, for $nL^2d > 1$, hydrodynamic interactions become increasingly insignificant and particle contacts become dominant. An example of this is shown in Figure 1-5. Here, the simulation outcomes shown include those of Salahuddin *et al.* [28] and Fan *et al.* [29]. These simulations incorporate long-range hydrodynamic and lubrication interactions, and particle contacts. Results of simulations by Snook *et al.* [30], also shown in Figure 1-5 indicate that the importance of including hydrodynamic interactions in the calculations of the microstructure lessens as the number density and aspect ratio increase. Collisions between the rods increases at the higher concentrations and dominate the hydrodynamic forces, which also become weaker at high values of $A$.

For the semi-dilute regime ($nL^2d \leq 1$), hydrodynamic interactions must be included in the simulations. For example, examining Figure 1-5 at $nL^2d = 1$ shows that the simulation predictions without hydrodynamic interactions are well below the experimental measurement and the other simulations. Simulations with short-range (lubrication), but without long-range, hydrodynamic interactions [31] are also shown. Interestingly, these results closely agree with those of Salahuddin *et al.* [28], suggesting that the long-range interactions have a weak effect on the orientation distributions even in the semi-dilute regime. Overall, more work is needed to definitively establish the relative effects of

the various interactions (hydrodynamic, short and long-range, and contacts) on the predictions of the microstructure in shear flows.

The work described in this dissertation aims to provide insight into the dynamics and rheology of concentrated suspensions of rigid rods with the aim of providing data to help resolve this question. This document is divided into two topics: comprehensive measurements of bulk rheological properties of a concentrated suspension of rigid rods using a custom-built rheometer (see Chapter 2), introduced in Subsection 1.3.1, and the investigation of collective motion of rigid rods due to an imposed oscillatory pipe flow (see Chapter 3), introduced in Subsection 1.3.2, showing the first experimental evidence of shear-induced migration of rods in pipe flows.

### 1.3.1 Rheology of Concentrated Suspensions

Though there have been numerical studies performed to understand the dynamics of concentrated suspensions, the results have been inconsistent. There is also a small amount of experimental work at high concentrations of fibers. It is this lack of experiments, and the lack of consistent corroboration between experimental work and theory, that motivate this project.

Despite the apparent simplicity of this system, several phenomena are observed that contradict expectations. A discrepancy identified from published works concerns the macroscopic rheology of concentrated suspensions. Suspensions of semi-concentrated and concentrated rods frequently exhibit shear-thinning behavior, and this behavior is more prominent at higher concentrations [33, 34]. However, theoretical analyses and numerical simulations suggest that the steady value of the viscosity of suspensions should be independent of the shear rate for non-colloidal, rigid rods suspended in Newtonian fluids [35, 36, 37]. Many hypotheses have been proposed to explain the origin of this anomalous shear thinning behavior seen in the experiments. These ideas range from questioning the Newtonian nature of the suspending fluid [38, 39] to the assertion that the fibers were not rigid under the imposed conditions [33, 40, 41]. In

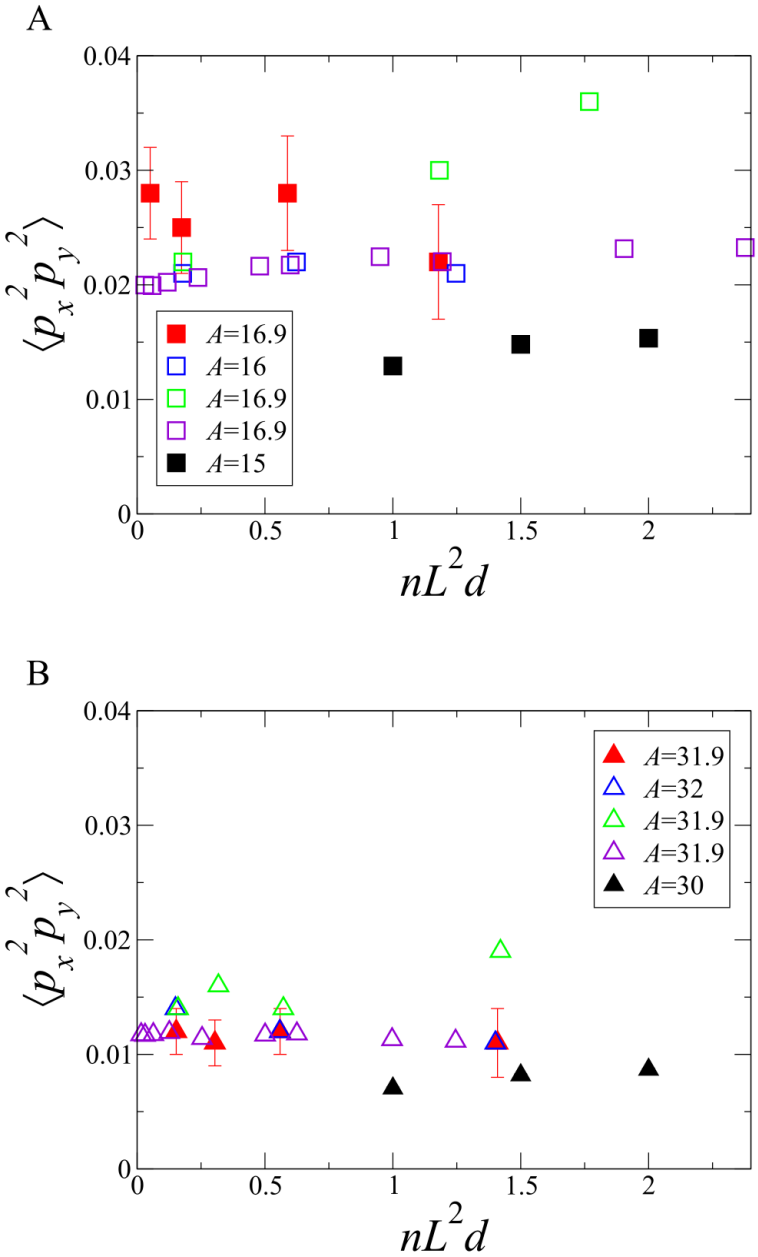


Figure 1-5. The fourth order moment of the orientation distribution, $\langle p_x^2 p_y^2 \rangle$, from experimental measurements and simulations for aspect ratios of A) $A \approx 16$ and B) $A \approx 32$. Experiments shown are those of Stover *et al.* [32] ($A = 16.9$ and 31.9, red); the simulations are those of Salahuddin *et al.* [28] (blue), Fan *et al.* [29] (green), Yamane *et al.* [31] (purple), and those from the simulations performed by Snook *et al.* [30] (black).

addition, we have very little information regarding the particle normal stresses in these suspensions.

Furthermore, there has been increasing interest in looking at the connection between the microstructure and the solid-transition state (i.e. jamming). This transition is represented by a sharp divergence in values of measured viscosity and occurs at concentrations where the mobility of the suspended particles is severely restricted, i.e. the suspension “jams”. A comprehensive analysis of phenomena and measurements at this jamming transition is lacking in the literature even for spheres, and there is little or no work on suspensions of non-spherical particles.

### 1.3.2 Shear-Induced Migration of Particles

Shear induced migration is the phenomena wherein particles are driven from a region of high shear to that of a lower shear. Leighton and Acrivos first observed this phenomena in experiments of particulate suspensions in a Couette viscometer [42]. This was a major breakthrough in understanding the rheology and dynamics of suspensions and led to many future studies. Karnis *et al.* [43] were the first group to observe migration of particles in a pipe flow. Since then several experiments have been conducted by various groups to observe migration in pressure-driven flows using various resonance imaging and velocimetry techniques [10, 44, 45, 46, 47, 48, 49].

At low Reynolds numbers, Stokes equations dictate that the fluid and particle motion is linear and reversible. However, at higher concentrations, various phenomena arise from irreversible dynamics. Shear induced migration is an example of these phenomena. There are a few hypotheses regarding the origin of these irreversibilities. One of the hypotheses is that there are particle-particle contacts, which could exist in conditions where there is a breakdown of the lubrication interactions between the particles. These contacts could arise from the presence of microscsopic deformations on the surface of the particles which cause deviations in the behavior of the particle dynamics from ideal smooth surfaces *viz.* the breakdown of the lubrication layer. These

short-ranged contact forces have been shown to cause non-reversible deviations in the trajectories of motion [50, 51, 52]. Another hypothesis is that the hydrodynamic multibody interactions, though formally reversible, are chaotic [53]. For spheres, the initial conditions had an insignificant effect on the chaoticity of the system, and hence could not account for the irreversibilities in the bulk behavior of the suspension. In suspensions of spheres, small perturbations to the particle motion, which are inevitably present are amplified through the non-linear hydrodynamic interactions and give rise to the irreversibilities despite the mathematical reversibility of the governing equations. However previous work done on spheres implied that the chaotic interactions could not explain the diffusion of spheres in sheared suspensions [54].

These works have focused on high volume fractions suspensions and the results reported were the measurements of the steady fully-developed flow profiles. One of the major complications in the viability of the abovementioned experiments is the need for high strain to observe any collective dynamics at Stokes flow conditions. To overcome this difficulty, an oscillatory flow can be used. For a large amplitude of oscillation, centerline migration was observed [44]. These studies have been limited to the dynamics of spherical particles. Mondy *et al.* [10] investigated the shear induced migration of rods, which was the first study of its kind for non-spherical particles. There is a distinct lack of experimental work to observe the collective irreversible dynamics of non-spherical particles in the literature, particularly for shear-induced migration, and this need primarily motivated a major portion of our work. Chapter 3 provides a detailed experimental study of shear induced migration of concentrated suspensions of rigid rods in an oscillatory pressure-driven flow.

# CHAPTER 2
# RHEOLOGY OF CONCENTRATED SUSPENSIONS OF RIGID FIBERS

The rheological properties of viscous Newtonian fluids containing rigid fibers remains relatively unexplored as compared to suspensions of spherical particles, and a consensus on even the qualitative description of the rheology is still lacking for concentrations beyond the dilute limit. As one example, the steady values of the shear stresses should, for suspensions of fibers that are large relative to colloidal scales and free of external body forces, follow a Newtonian law [35]. However, many experimental studies find yield stresses and a nonlinear scaling of the shear stresses with the rate of shear, where these non-Newtonian effects become more prominent with increasing concentration [33, 55]. Different explanations have been proposed to explain the departure from a Newtonian response. This includes arguments that the fibers were not rigid under the imposed conditions [33, 40], or that the fibers are not force-free. An example of the latter is the assertion that adhesive forces can exist between the fibers, even though their size is large compared to typical colloidal scales [56, 57, 58].

Previous rheological studies have focused on suspensions at relatively small volume fractions. Identifying measurements of rheology for volume fractions, $\phi$, above 0.1 is difficult for fibers of aspect ratios $A = L/d > 20$, where $L$ and $d$ are the fiber length and diameter, respectively. The lack of data is attributable, at least in part, to the difficulty of preparing and measuring the rheology of suspensions at high concentrations for large aspect ratios. Even for moderate aspect ratios of around 17 or 18, measurements are available for volume fractions of only up to $\phi = 0.15$ or 0.17 [59, 60]; measurements as high as $\phi = 0.23$ were made by Bibbo *et al.* [60] for smaller aspect ratios of $A = 9$. As a result, the rheological properties of suspensions of rigid fibers remains to be characterised in the limit of large concentrations where mechanical contacts are expected to matter [11, 61, 62]. Likewise, the volume fraction at which the shear stresses diverge,

and the flow of the suspension ceases (i.e. becomes jammed), has not been determined previously.

Here, a custom-built rheometer has been used to explore the shear stresses and normal forces in suspensions of non-colloidal, rigid fibers for concentrations exceeding $\phi = 0.23$. The rheometer measures the stresses in both a pressure and volume-imposed configuration [63, 64]. The measurements indicate the presence of yield stresses in the tested suspensions, but also a viscous scaling wherein the stress grows linearly with the rate of shear. The unique rheometer design facilitates the study of these highly concentrated suspensions of fibers, and, for the first time to our knowledge, the volume fractions at which the stresses diverge are measured. The scaling of the stresses near this jamming transition are found to differ substantially from that of a suspension of spheres. These measurements are reported in Section 2.2, after presenting the experimental materials and techniques in Section 2.1; conclusions are drawn in Section 2.3.

## 2.1 Experiments

The objectives of the experimental work are to characterize the rheology of highly concentrated suspensions of rigid rods by the measurement of parameters like viscosities, friction coefficients, and volume fractions; to make the first measurements of particle pressures of suspensions of rigid rods at high concentration; and to form constitutive laws to model the rheology near the jamming transition. To enable these objectives, experiments have been performed in a modified rheometer of original design. This rheometer setup consists of a wide-gap annular shear cell, with a movable top plate. Various supporting devices are installed for direct measurements, control, and interfacing with a computer.

### 2.1.1 Particles and Fluid

Four batches of rod-like particles were used in the experiments. They were obtained by using a specially-designed device to cut long cylindrical filaments of plastic

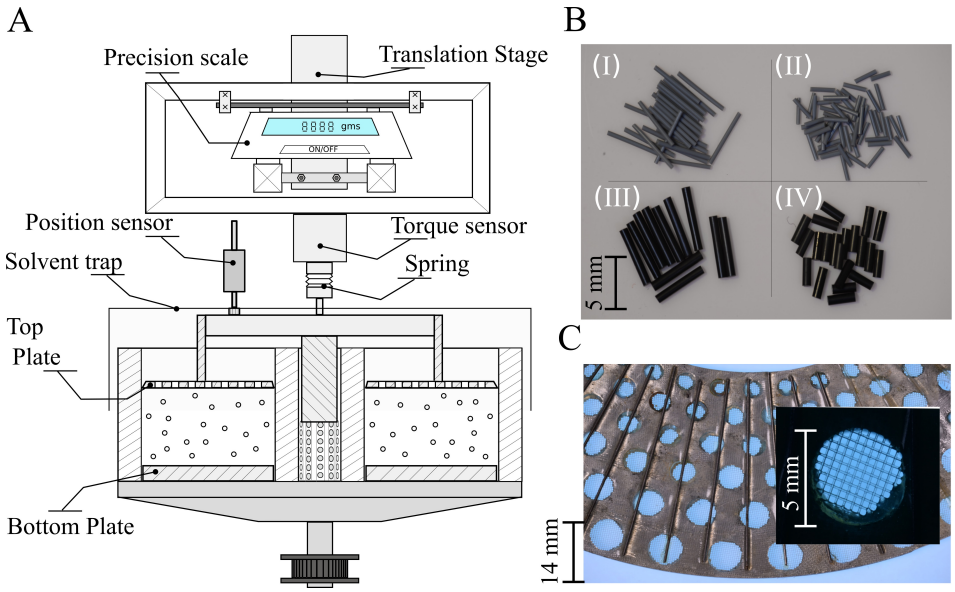


Figure 2-1. Experimental setup for measuring rheological parameters near the jamming limit, microscope image of the fibers, and zoomed-in image of the porous top-plate. A) Sketch of the experimental apparatus. See Appendix B for an additional schematic of the rheometer. B) Microscopic images of the plastic fibers. C) Image of the top plate (the inset is a blowup of the image showing the nylon mesh).

Table 2-1. Properties of each batch of fibers. Data shown includes the mean value and standard deviation of the aspect ratio $A$, fiber length $L$, and fiber diameter $d$. Values of the dimensionless number $S_p$, characterising the relative strengths of the viscous and elastic forces, are also reported.

| Fiber label | Symbol | $A$ | $L$ (mm) | $d$ (mm) | $S_p$ |
|---|---|---|---|---|---|
| (I) | □ | $14.5 \pm 0.8$ | $5.8 \pm 0.1$ | $0.40 \pm 0.01$ | $5 \cdot 10^{-3}$ |
| (II) | △ | $6.3 \pm 0.4$ | $2.5 \pm 0.1$ | $0.40 \pm 0.01$ | $2.4 \cdot 10^{-4}$ |
| (III) | ◇ | $7.2 \pm 0.4$ | $5.8 \pm 0.2$ | $0.81 \pm 0.02$ | $3.9 \cdot 10^{-4}$ |
| (IV) | ◯ | $3.4 \pm 0.3$ | $2.8 \pm 0.1$ | $0.81 \pm 0.03$ | $2.7 \cdot 10^{-5}$ |

(PLASTINYL 6.6) that were supplied by PLASTICfiber S.P.A. (http://www.plasticfiber.com). Images of typical fibers from each batch are shown in Figure 2-1 (b). The length and diameter of over 100 fibers were measured with a digital imaging system. The distributions of lengths and diameters were found to be approximately Gaussian for all aspect ratios. The mean value and standard deviation of the fiber aspect ratio $A = L/d$, length $L$, and diameter $d$ are shown in Table 2-1. Note that batches (II) and (III) have very different lengths and diameters, but roughly the same aspect ratio of $A \approx 6 - 7$.

The rigid fibers were suspended in a Newtonian fluid that had a matching density of $\rho_f = 1056$ kg/m$^3$. The suspending fluid was a mixture of water ($10.72$ wt$\%$), Triton X-100 ($75.78$ wt$\%$), and Zinc Chloride ($13.50$ wt$\%$). The fluid viscosity of $\eta_f = 3$ Pa·s and the density were measured at the same temperature ($25°$C) at which the experiments were performed. The suspensions were prepared by adding the fibers to the fluid, where both quantities were weighed, and gently stirring. Little to no settling or creaming was observed.

The rheological measurements were performed at a maximum shear rate of $\dot{\gamma} \approx 3$ s$^{-1}$, ensuring that a maximum Reynolds number ($\rho_f \dot{\gamma} L^2/\mu_f$) of 0.04 was achieved. The fibers can be considered non-colloidal, owing to their large size, and rigid under the conditions of the experiment. Regarding the latter, the buckling criterion has been characterised by a dimensionless number, $S_p = 128\, \eta_f \dot{\gamma}\, A^4/E_Y \ln(2A)$, where the Young's modulus, $E_Y$, is approximately 3000 MPa for PLASTINYL 6.6. The number $S_p$, often called the sperm number, is a ratio of the viscous and elastic forces acting on the fiber [65]. The values of $S_p$, shown in Table 2-1 for our experiments, were much smaller than the critical Sperm number of $328$ for the coil-stretch transition in a cellular flow [66]. A more detailed overview of testing rigidity of rod shaped particles is described in Appendix A.

### 2.1.2 Pressure Imposed Rheometer Setup

The experiments were conducted using a custom rheometer that was originally constructed by Boyer *et al.* [63] and then modified by Dagois-Bohy *et al.* [64]. This rheometer, sketched in figure 2-1 (a), provides measurements of both shear and normal stresses. The shearing cell consists of (i) an annular cylinder (of radii $R_1 = 43.95$ mm and $R_2 = 90.28$ mm) which is attached to a bottom plate that can be rotated and (ii) a top cover plate that can be moved vertically. This top plate is porous, enabling fluid to flow through it, but not particles. The plate was manufactured with holes of sizes $2 - 5$ mm and then was covered by a 0.2 mm nylon mesh (see Figure 2-1 (c)). The parallel bottom and top plates have also been roughened by positioning regularly-spaced stripes of height and width 0.5 mm onto their surfaces. A transparent solvent trap covers the cell, hindering evaporation of the suspending fluid.

Experiments were carried out in two modes, *viz.* volume-controlled mode and pressure-controlled mode. The former is akin to conventional rheometry, where the volume of the cell is fixed for each run, hence the volume fraction of the suspension is defined for each run. The latter is a novel way of performing these types of experiments, drawing from concepts in granular rheology. In pressure-imposed rheometry, the particle pressure $P$ is maintained at a set value that is measured by the precision scale; the volume fraction $\phi$ and the shear stress $\tau$ are measured as a function of the shear rate $\dot{\gamma}$ and pressure $P$. In volume-imposed rheometry, the height $h$, and consequently the volume fraction $\phi$, are maintained at a fixed value, while the shear stress, $\tau$, and particle pressure, $P$, are measured as a function of the shear rate, $\dot{\gamma}$. See Appendix B for a detailed analysis of the measured quantities and calculated values. Errors in the measurements of $\tau$, $P$, and $\phi$ for the suspensions depend upon the calibration experiments, the preparation of the suspension samples, and the precision of the height, torque, and scale measurements. Estimates, based upon tests with independently

created samples of suspension, suggest errors of $\pm 6$ Pa, $\pm 5$ Pa, and $\pm 0.005$ for $\tau$, $P$, and $\phi$, respectively.

In a typical experiment, the annular cell was filled with suspension and the porous plate was lowered into the fluid to a position $h$. This height, measured independently by a position sensor (Novotechnik T-50), provides the information necessary to calculate the fiber volume fraction, $\phi$. The bottom annulus was rotated at a rate $\Omega$ by an asynchronous motor (Parvalux SD18) regulated by a frequency controller (OMRON MX2 0.4 kW), while the torque exerted on the top plate was measured by a torque transducer (TEI – CFF401). The shear stress $\tau$ was deduced from these torque measurements after calibration with a pure fluid to subtract undesired contributions resulting from the friction at the central axis and the shear in the thin gap between the top plate and the cell walls. A precision scale (Mettler-Toledo XS6002S) measured the apparent weight of the top plate and, after correcting for buoyancy and normalisation by the area, provided the determination of the normal stress acting in the gradient direction. For simplicity, this is referred to as the particle pressure, $P$. The scale was placed on a vertical translation stage driven by a LabVIEW code.

Figure 2-2 shows sample data sets for the suspending fluid in the absence of particles, suspension in volume-controlled and pressure-controlled experiments respectively. Steady state values were obtained using the signals obtained from the transducers. Corrections are made to the values obtained by means of calibration experiments carried out using only the suspending fluids. These calibrations are carried out every time the suspending fluid is changed. These values were used to calculate and plot various characteristic curves. A detailed explanation for the calibration and the data analysis is provided in Appendix B. Shear and normal viscosities were calculated using Equation C-5.

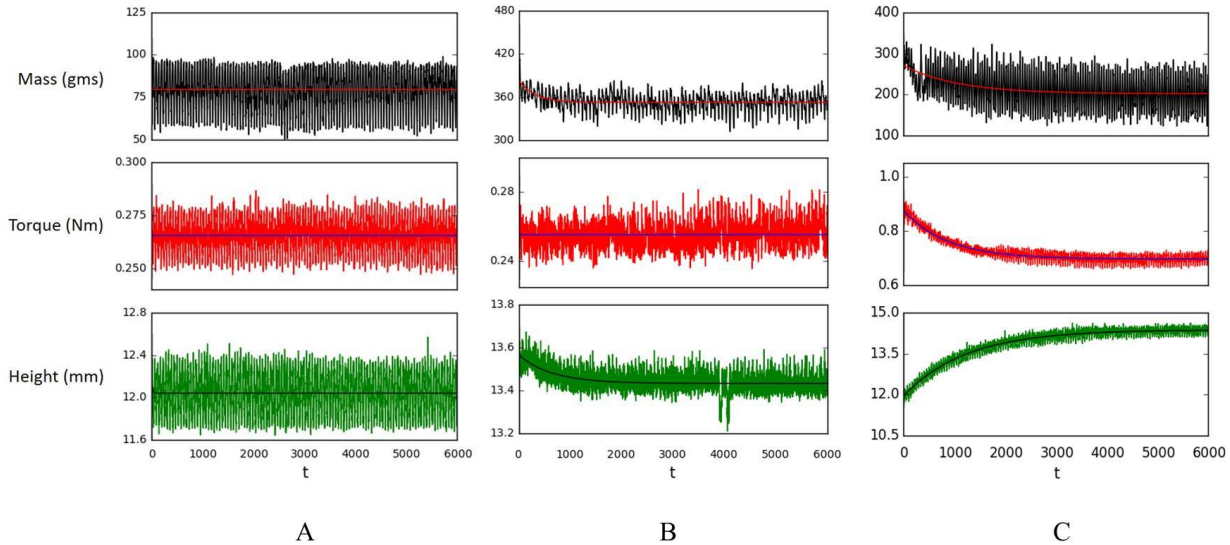


Figure 2-2. Raw data supplied by the shear cell for fibers of aspect ratio, $A$ =11.3. A) pure suspending fluid which is run in volume-control mode, B) volume-control mode data for the suspension, and C) pressure-control mode data for the suspension.

## 2.2 Results and Discussion

### 2.2.1 Shear and Normal Viscosity

Typical rheological data for the apparent relative shear and normal viscosities, $\tau/\eta_f\dot{\gamma}$ and $P/\eta_f\dot{\gamma}$, are plotted against volume fraction, $\phi$, in Figure 2-3 (a) and (b). The data was collected for fibers of batch (II) using pressure-imposed and volume-imposed measurements. As expected, both quantities increase with increasing $\phi$. However, multiple values of the apparent viscosities are measured for any given $\phi$. Plotting the shear stress, $\tau$, and the particle pressure, $P$, against the shear rate for different values of $\phi$ demonstrates that $\tau$ and $P$ are linear in $\dot{\gamma}$, but have a non-zero value at $\dot{\gamma} = 0$, see Figure 2-3 (a) and (b). This seems to suggest that a yield-stress exists for both the shear stress and the particle pressure, $\tau_0$ and $P_0$, respectively. Their values can be determined using a linear fit of the stress and pressure data as a function of $\dot{\gamma}$, as indicated by the lines in Figure 2-4 (a) and (b). Both yield-stresses, $\tau_0$ and $P_0$, increase

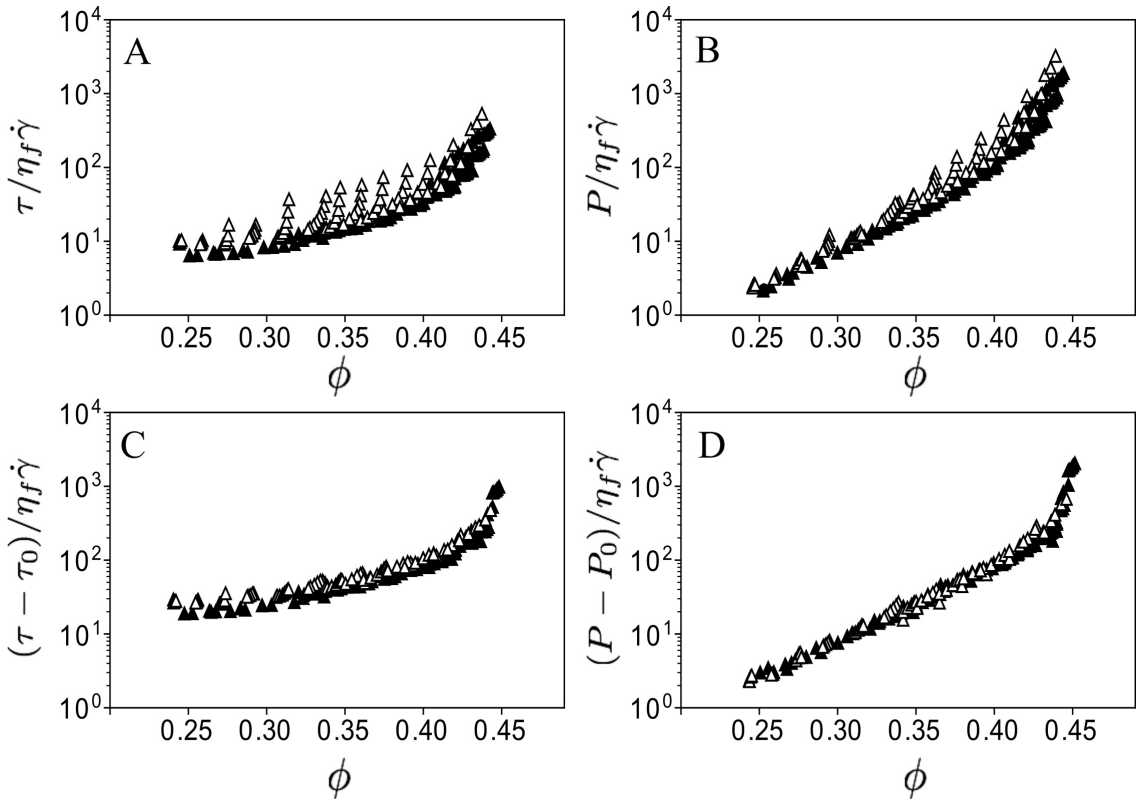


Figure 2-3. Shear and normal rheology analyses. A) Shear ($\tau/\eta_f\dot{\gamma}$)) and B) normal ($P/\eta_f\dot{\gamma}$) viscosities as a function of volume fraction, $\phi$. Panels C) and D) show shear [$(\tau-\tau_0)/\eta_f\dot{\gamma}$] and normal viscosities [$(P-P_0)/\eta_f\dot{\gamma}$], as a function of volume fraction, after subtraction of the yield stresses. Experiments were conducted in both pressure-imposed (▲) and volume-imposed (△) modes.

with increasing $\phi$ as shown in Figures 2-4 (c) and (d) for all four batches of fibers. The growth in $\tau_0$ and $P_0$ with respect to $\phi$ are more pronounced for larger aspect ratios $A$.

The data of Figure 2-4 (a) and (b) demonstrate that the stresses scale linearly with the rate of shear, as expected. Furthermore, the slopes of $\tau$ and $P$ with $\dot{\gamma}$ increase with $\phi$, which is evidence of the increase of the shear and normal viscosities with $\phi$. These shear and normal viscosities can be collapsed into a single function of $\phi$ by removing the yield stresses. Figures 2-4 (c) and (d) show the results of $(\tau-\tau_0)/\eta_f\dot{\gamma}$ and $(P-P_0)/\eta_f\dot{\gamma}$ as a function of $\phi$. In all of the following analysis, the yield stresses are subtracted systematically from the raw data.

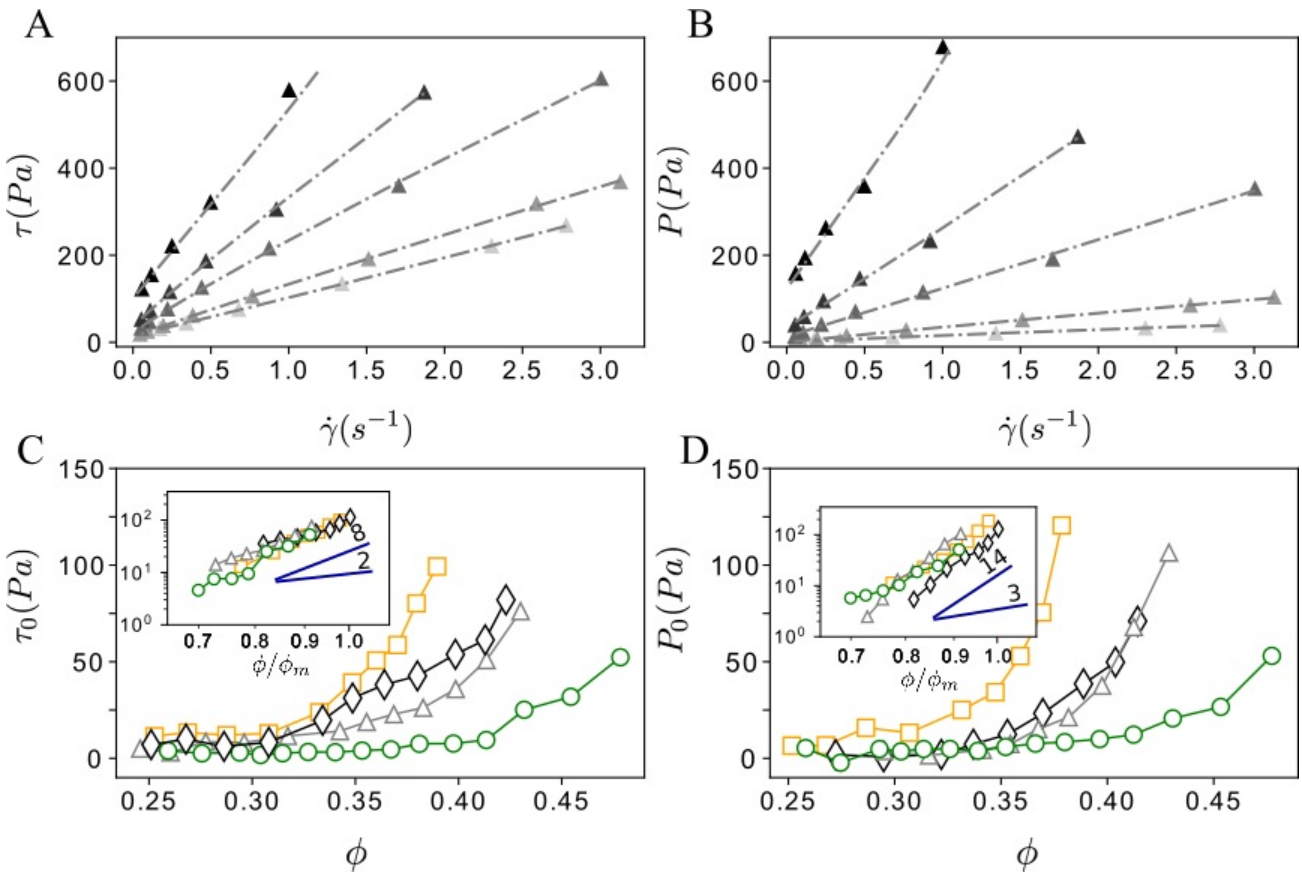


Figure 2-4. Shear stress and particle pressure data. A) Shear stress ($\tau$) and B) particle pressure ($P$) versus shear rate, $\dot{\gamma}$, for the fiber suspension of batch (II) at different $\phi$ values of 0.26 (lightest grey shade), 0.30, 0.35, 0.38, and 0.41 (black). The lines represent the linear fit for each different $\phi$ value. Yield-stress C) for the shear stress ($\tau_0$) and D) particle pressure ($P_0$) versus $\phi$ for fibers of batch (I), (II), (III), and (IV) shown using the symbols □, △, ◇, and ◯, respectively (see table 2-1). The insets of graphs (c) and (d) are log-log plots versus $\phi/\phi_m$ where $\phi_m$ is the maximum flowable volume fraction given in figure 2-6 (a).

### 2.2.2 Analysis of Near-Jamming Limit Rheology

Figures 2-5 (a) and (b) show the relative shear ($\eta_s = (\tau - \tau_0)/\eta_f\dot{\gamma}$) and normal ($\eta_n = (P - P_0)/\eta_f\dot{\gamma}$) viscosities for all of the fiber batches. Both quantities increase with $\phi$ and seem to diverge at a maximum volume fraction that depends on the aspect ratio $A$. The influence of the aspect ratio is also seen on the rheological functions as $\eta_s(\phi)$ and $\eta_n(\phi)$ shift toward lower values of $\phi$ with increasing $A$. An interesting observation is that the data for batches (II) and (III), corresponding to similar values of $A$ but different sizes,

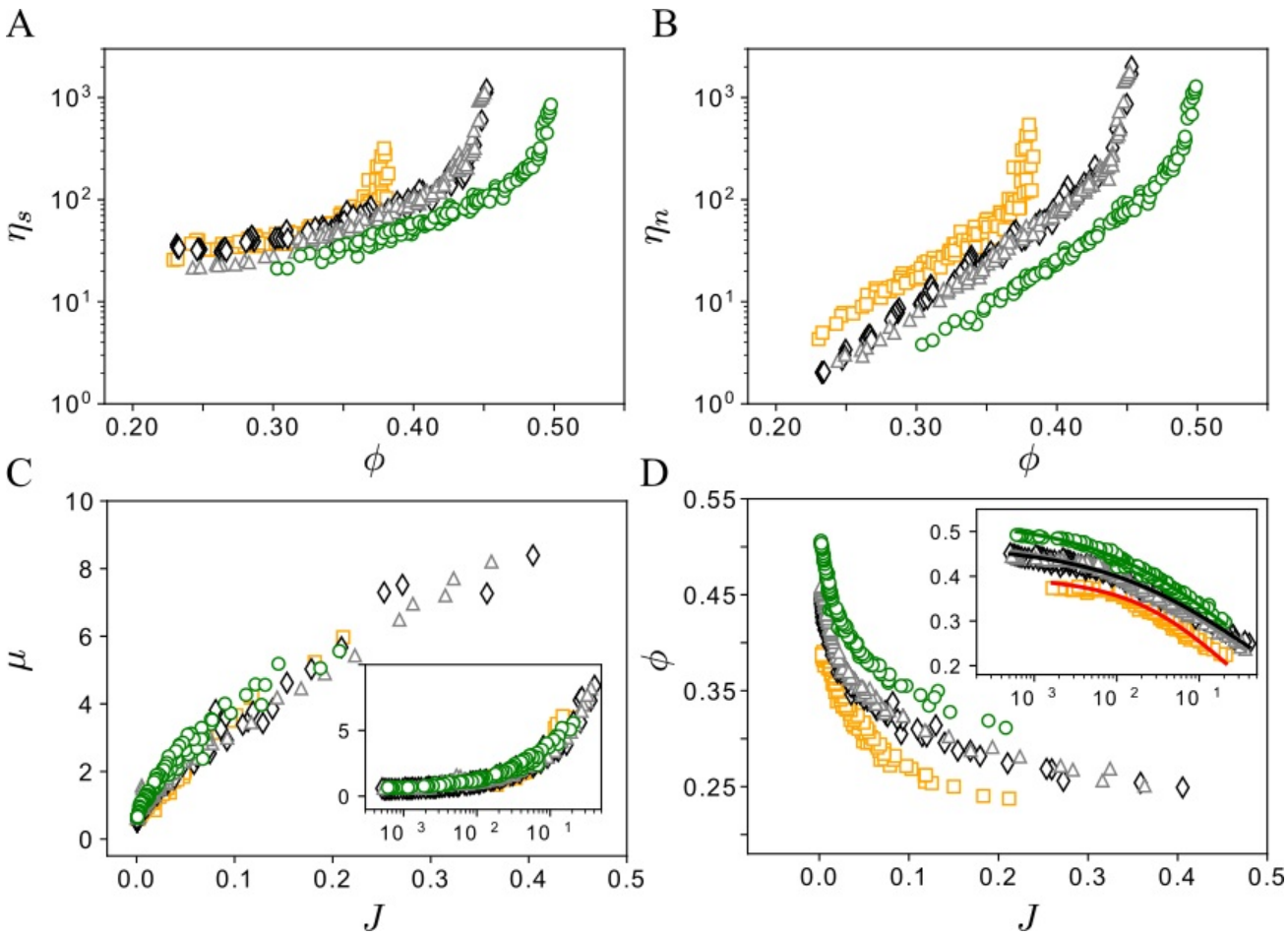


Figure 2-5. Comparisons of shear viscosity ($\eta_s$) vs. volume fraction ($\phi$) and normal viscosity ($\eta_n$) to dimensionless shear rate $J$. A) $\eta_s = (\tau - \tau_0)/\eta_f\dot{\gamma}$ and B) $\eta_n = (P - P_0)/\eta_f\dot{\gamma}$ versus $\phi$ as well as C) $\mu = \eta_s/\eta_n$ and D) $\phi$ versus $J = \eta_f\dot{\gamma}/(P - P_0)$, for fiber batches (I), (II), (III), and (IV) as represented by the symbols □, △, ◇, and ◯, respectively (see Table 2-1). The insets of graphs C) and D) are logarithmic plots.

collapse onto the same curve. This indicates that finite size effects are not significant. Also, the decrease of $\eta_n$ is much stronger than that of $\eta_s$ for $\phi \lesssim 0.35$.

An alternative representation of the rheological data plots the friction coefficient $\mu = \eta_s/\eta_n$ and the volume fraction $\phi$ as a function of the dimensionless shear rate, $J = \eta_f\dot{\gamma}/(P - P_0)$ [63]. The rheology is then described by the two functions $\mu(J)$ and $\phi(J)$ as shown in Figure 2-5 (c) and (d) for the same data as in Figure 2-5 (a) and (b) (refer Appendix C). A striking result is that a complete collapse of all the data is observed for $\mu(J)$, indicating that the friction coefficient is independent of the aspect

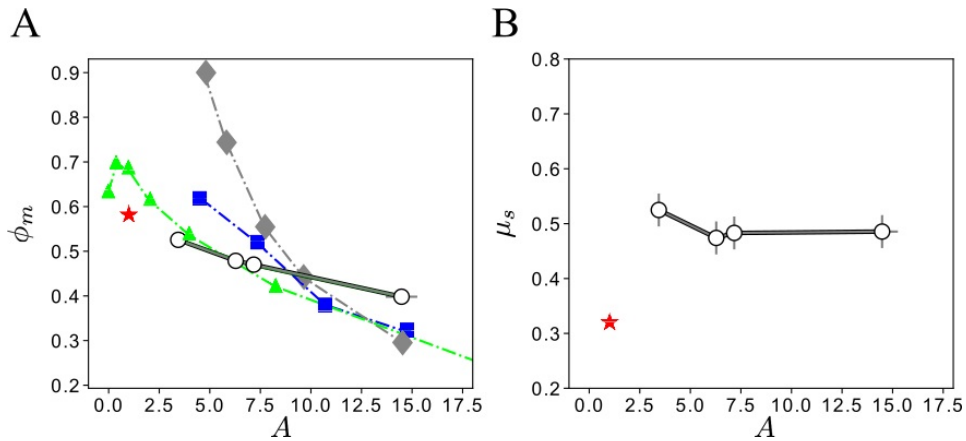


Figure 2-6. Critical values of volume fraction and friction near the jamming limit. A) $\phi_m$ (◯) and B) $\mu_s$ (◯) at the jamming point versus fiber aspect ratio, $A$, together with the data (★) obtained by Boyer *et al.* [63] for suspensions of spheres ($A = 1$). Comparisons with experimental data from Rahli *et al.* [67] (■) on the dry packing of rigid fibers and the simulations of Williams & Phillipse [68] (▲) for the maximum random packing of spherocylinders are given on graph A).

ratio $A$. The volume fraction $\phi$ is a decreasing function of the dimensionless number $J$. There is a clear shift of $\phi(J)$ toward the lower values of $\phi$ when $A$ is increased. The data for batches (II) and (III), having similar aspect ratios, again collapse onto the same curve.

This frictional approach is particularly well suited to study the jamming transition, as it circumvents the divergence of the viscosities. From the logarithmic plot of $\phi(J)$, shown in the inset of figure 2-5 (d), the critical (or maximum flowable) volume fraction $\phi_m$ can be determined from the limiting value of $\phi$ as $J$ goes to zero. Similarly, the logarithmic plot of $\mu(J)$ in the inset of figure 2-5 (c) shows that the friction coefficient tends to a finite value $\mu_s$ at the jamming point.

The critical values $\phi_m$ and $\mu_s$ are plotted against the fiber aspect ratio $A$ in figures 2-6 (a) and (b), respectively. Again, the similar results for batches (II) and (III) indicate that confinement is not influencing the measurements, and the values obtained by [63] for suspensions of spheres are also plotted on these graphs (for $A = 1$, although strictly speaking a sphere is not a cylinder of aspect ratio one). Clearly, $\phi_m$ decreases

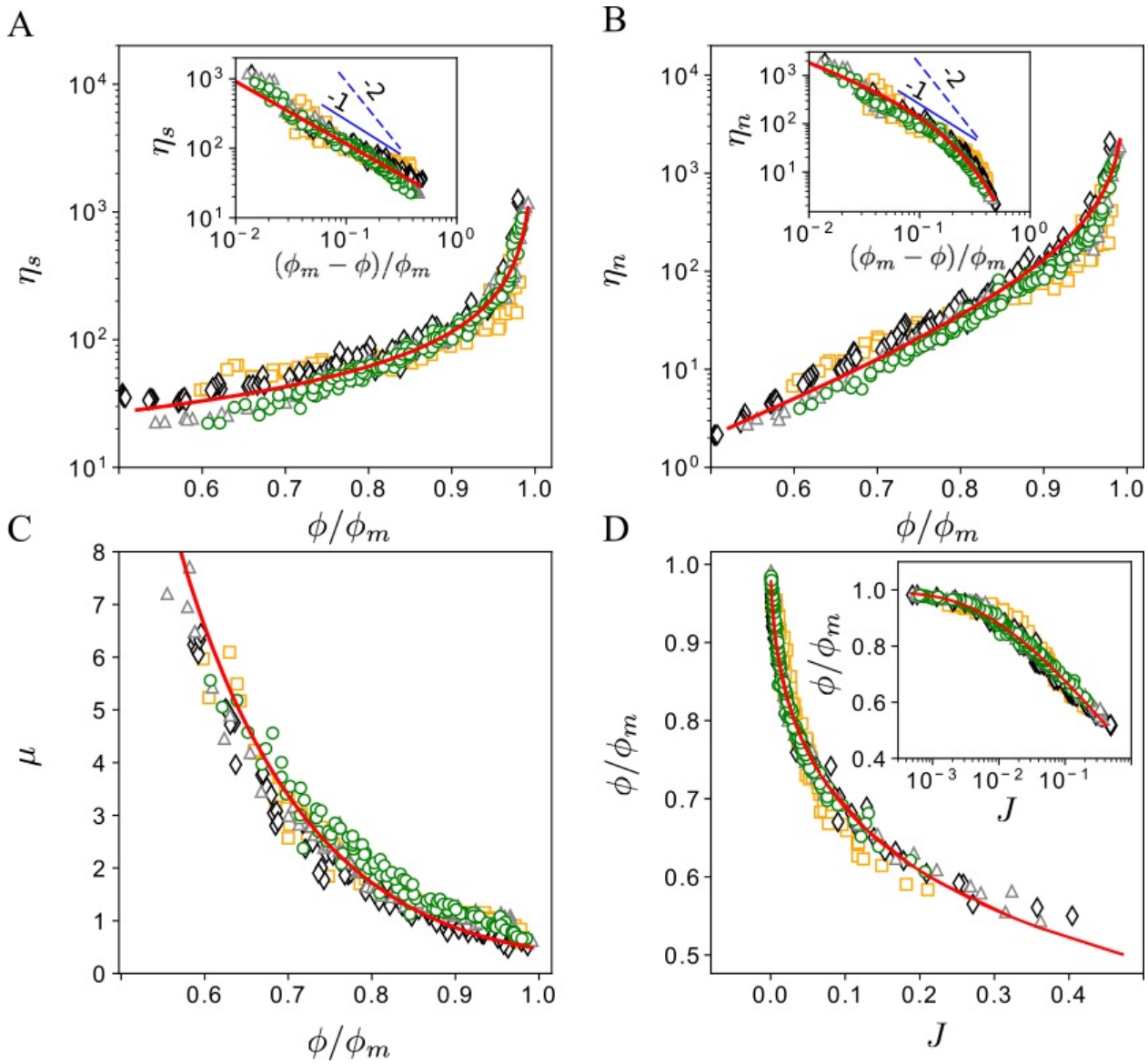


Figure 2-7. Rescaled rheological data: A) $\eta_s = (\tau - \tau_0)/\eta_f\dot{\gamma}$, B) $\eta_n = (P - P_0)/\eta_f\dot{\gamma}$ and C) $\mu = \eta_s/\eta_n$ versus $\phi/\phi_m$ as well as D) $\phi/\phi_m$ versus $J = \eta_f\dot{\gamma}/(P - P_0)$, for all the data of the different batches (I), (II), (III), and (IV) shown using the symbols □, △, ◇, and ◯, respectively (see table **??**). The insets of graphs (a), (b), and (d) are log-log plots. The red solid curves correspond to the rheological laws given by equations (2–1), (2–2), and (2–3).

with increasing $A$. This follows the general trends of a decrease in volume fraction with the aspect ratio for processes such as dry packing, as shown in Figure 2-6 (a). A comparison is also made in Figure 2-6 (a) between the values of $\phi_m$ and estimates from simulations [68] of the maximum concentration at which the orientation distribution remains random. The critical friction $\mu_s$ does not vary significantly with $A$ in the explored range and its value ($\approx 0.47$) is larger than that obtained for spheres ($\approx 0.32$) [63].

Figure 2-7 displays the same data as figure 2-5, but with $\phi$ scaled by $\phi_m$. This simple rescaling leads to a good collapse of the data for all of the fiber batches, indicating that the aspect ratio principally impacts the maximum volume fraction, $\phi_m$. Another remarkable result is that the relative shear and normal viscosities, $\eta_s$ and $\eta_n$, diverge near the jamming transition with a scaling close to $(\phi_m - \phi)^{-1}$, as clearly evidenced by the insets of figures 2-7 (a) and (b). This starkly contrasts with the divergence of $(\phi_m - \phi)^{-2}$ observed for suspensions of spheres [63].

A constitutive law for $\mu$ can be generated by fitting the data to a linear combination of powers of $(\phi_m - \phi)/\phi$,

$$\mu(\phi) = \mu_s + \alpha \left( \frac{\phi_m - \phi}{\phi} \right) + \beta \left( \frac{\phi_m - \phi}{\phi} \right)^2, \tag{2–1}$$

was done for spheres [64]. The red curve in figure 2-7 (c) shows the result, with $\mu_s = 0.47$, $\alpha = 2.44$, and $\beta = 10.20$. As noted previously, the value for $\mu_s$ is larger than that obtained for suspensions of spheres ($\mu_s = 0.3$). The values for $\alpha$ and $\beta$ also differ from those obtained for suspensions of spheres ($\alpha = 4.6$ and $\beta = 6$). The best fit for $\eta_s$ was found to be

$$\eta_s(\phi) = 14.51 \left( \frac{\phi_m - \phi}{\phi_m} \right)^{-0.90}, \tag{2–2}$$

as seen in figure 2-7 (a). Note that the best-fit exponent is $-0.9$, rather than $-1$. The rheological law for $\eta_n$ is then just given by

$$\eta_n(\phi) = \eta_s(\phi)/\mu(\phi), \tag{2–3}$$

which is represented by the red curve in figure 2-7 (b). The variation of $\phi$ with $J$ can be deduced from this last law since $J = 1/\eta_n(\phi)$; this result is shown in Figure 2-7 (d).

### 2.2.3 Observation of Yield Stresses

The suspensions exhibit yield-stresses which increase with increasing volume fraction, $\phi$, and are more pronounced for larger aspect ratios. Yield-stresses have been reported previously for rigid fibers suspended in Newtonian fluids, and the yield stresses have been attributed to adhesive contacts [56, 57] despite the relatively large size of the fibers. A recent model [58], which considered attractive interactions between fibers in the dilute regime, predicted simple Bingham laws for both the shear stress and the first normal stress difference, with the apparent shear and normal yield stresses proportional to $\phi^2$ and $\phi^3$, respectively. The present data also follows Bingham laws, but the yield stress, $\tau_0$, and pressure, $P_0$, increase with higher power laws in $\phi$ than predicted. This can be seen in the insets of figures 2-3 (c) and (d), where it is also demonstrated that the data for all aspect ratios collapses onto single curves by rescaling $\phi$ by $\phi_m$.

It is unclear whether, for the large fibers used here, colloidal forces are responsible for the yield-stresses. Finite-size effects close to the jamming point can also be advocated, particularly since lubrication forces are inefficient at preventing mechanical contacts between elongated particles [61]. Close to jamming, since the system has a finite size, percolating jamming network of particles can exist. While it is transient phenomenon, it may impact the averaged rheological measurements which consequently may exhibit apparent yield stresses. Clearly, more work is necessary to elucidate the origin of the yield stresses.

## 2.3 Conclusions

Using a custom rheometer we have performed pressure and volume-imposed measurements of the rheology of non-colloidal rigid fibers suspended in a Newtonian fluid. Measurements for the shear stress and particle pressure have been obtained in

the dense regime and for aspect ratios between 3 and 15, and the volume fractions at which the rheology diverges has been characterised as a function of the aspect ratio.

Subtracting the apparent yield-stresses reveals a viscous scaling for both the shear stresses and particle pressures, wherein both grow linearly with the rate of shear. The aspect ratio of the fibers does not affect the friction coefficient, $\mu$, but does impact the maximum flowable volume fraction, $\phi_m$. Rescaling the volume fraction, $\phi$, by this maximum volume fraction, $\phi_m$, leads to an excellent collapse of all the data on master curves for the shear and normal viscosities. Hence, we argue that the aspect ratio principally affects the maximum volume fraction at which the suspensions can be sheared.

Using the data presented here, constitutive laws in the form of expansions in $(\phi_m - \phi)$ have been generated for the rheology of dense suspensions of rigid fibers. An important product of the present study is the examination of the rheology close to the jamming transition. At jamming the friction coefficient is found to be constant and to be larger than that found for suspensions of spheres. Both shear and normal viscosities present a similar algebraic divergence in $\approx (\phi_m - \phi)^{-1}$ in stark contrast to that in $(\phi_m - \phi)^{-2}$ observed for suspensions of spheres near the jamming point. The maximum volume fraction $\phi_m$ is seen to decrease with increasing aspect ratio, similar to the dry packing of rigid fibers found in experiments [67], see figure 2-6 (a). However, no inferences about the general structure of the suspension at jamming is possible, as comparisons with estimates of maximum random packing do not clearly indicate that the orientation distribution has organized [68]. Direct observations, or simulations, of the structures need to be developed in future work to resolve this question.

# CHAPTER 3
# DYNAMICS OF CONCENTRATED SUSPENSIONS OF RIGID FIBERS

An individual fiber that is rigid and free of any external forces exhibits reversible motions when suspended in a viscous fluid, so long as the rate of flow remains low. For example, such a fiber flowing through a cylindrical tube in response to an oscillating pressure gradient will return to its initial position and orientation after each cycle. However, measurements described in this paper demonstrate that the spatial and orientational distribution of a concentrated suspension of rigid and force free fibers is not reversible during flow through a tube. Rather, the results indicate that particles preferentially migrate toward the center of the tube, with the extent of migration depending upon the amplitude of the oscillatory displacement in the tube and the concentration of the fibers.

The migration of the rigid fibers during tube flow is an expected, even if previously undemonstrated, result, as the identical phenomenon for suspensions of spheres has been studied extensively. The general observation, first made by Leighton & Acrivos [6], is that spheres migrate from regions of high shear to low shear occurs until balanced by the tendency of the spheres to migrate from regions of high concentration to lower concentration. Furthermore, the rates of migration scale with the rate of shear and are independent of the viscosity of the suspending fluid if the Reynolds number remains low. This shear-induced migration has been observed in Couette geometries [6, 69, 70, 71], in pressure-driven flows [43, 45, 46, 47, 48], and for flow betweeen rotating eccentric cylinders [72]. In the more specific case of oscillatory flow for suspensions of spheres in a tube [44, 73], the detailed migration results were found to depend upon the strain amplitude and concentration.

The shear-induced migration of particles signifcantly impacts the operation of flow processes. The migration of spheres in a Couette geometry affects the rheological measurements of suspensions, complicating the evaluation of the effective viscosity [5].

In this geometry, spheres migrate away from the region of high shear in the gap between the cup and bob toward the region below the bob where the shear rate goes to zero. Consequently, the torque measured by the rheometer changes in time and the steady, long-time measurement is not representative of the viscosity of the suspension at the desired concentration. As another example, the migration of particles to the center of the pipe in a pressure-driven flow result in a pressure drop that is no longer linear along the length of the pipe and that is lower than expected owing to the lower effective viscosity near the bounding walls.

The origin of particle migration represents a fundamental, unresolved problem, as the governing equations for the fluid (Stokes equations) and particle motion are formally reversible and migration should not occur. Two ideas, both of which could be operating simultaneously, have been advanced to resolve this question. The first attributes the irreversible motion to the chaoticity of the hydrodynamic interactions between the particles [53]. In this scenario, the small perturbations to the particle motion, which are inevitably present in real suspensions, are amplified through the nonlinear interactions and give rise to the migration despite the mathematical reversibility of the governing equations. The second idea is that particle contact-collisions drive the irreversible migration [6]. This introduces an irreversible component into the governing equations, but requires relaxation of the traditional assumption made in Stokes flow that lubrication forces prevent particle surfaces from touching. Experimental evidence supports the idea that particle-particle contacts alter the the extent of irreversibility in concentrated suspensions [74, 75]. Experiments have yet to be performed, however, that directly correlate particle migration with the particle roughness. Numerical evidence from simulations support the idea that chaotic hydrodynamic interactions drive irreversible particle distributions during sedimentation [76], but not during the shear flow of force free particles [77, 78] where the interactions are weaker.

Along with experimental evidence of shear induced migration in concentrated suspensions of spheres, numerical simulations also predict similar collective behavior of particles. Monolayer simulations of spheres in a pressure-driven flow between two plane walls using the Stokesian Dynamics method [9] agreed qualitatively with the experimental observations and also verified many assumptions regarding shear-induced migration, including the fact that the phenomenon is not due to inertial effects. More recent studies have expanded to three-dimensional simulations of concentrated suspensions of thousands of particles of monodisperse non-colloidal particles in tube flow [79].

Continuum models have been developed to predict particle migration as well. Early models of shear-induced migration posited a phenomenological equation for predicting the particle distribution. In these diffusion models [6, 8], particle migration is modeled as a diffusive flux. Phillips et al. [8] defined two fluxes influencing particle migration. The first flux is based on the collision frequency of particles and describes a flux from high to low shear rates (first term), and a counterflux generated by an increased concentration of particles (second term). This flux depends on the particle radius, shear rate, and the concentration of particles. A second flux, reflects a motion of particles from low to high shear rate zones due to the increased viscosity caused by increases in particle concentration. The flow field must be determined from the Stokes equation, where the viscosity varies spatially according to the concentration of particles. Models of suspension viscosity, such as the Krieger-Dougherty model [80], can be used for this purpose. The diffusion model successfully predicts the existence of migration in wide-gap Couette and pressure-driven Poiseuille flows, and the predictions are in agreement with measurements that indicate that the concentration profile is independent of the applied shear rate and independent of the viscosity of the suspending medium. However, the diffusion model is applicable strictly for unidirectional flows and the model fails to predict the absence of a net migration in curvilinear torsional flows [81].

A more recent model relates the migration flux and rheology of the suspension [9, 82]. This suspension balance model is a two-phase model which provides a continuum description of the bulk suspension motion, as well as the relative velocity of the particle phase and fluid phase. The model is systematically derived by performing a phase average of the governing momentum and continuity equations. According to this model, the migration flux is driven by the divergence in the normal stress of the particle phase, which has recently been argued to include the contact or interparticle contributions as well as hydrodynamic contributions coming from the non-drag portion of the interphase force [83, 84]. This equation must be solved in conjunction with the overall momentum equation for the suspension. The suspension balance model has a number of potential advantages over the diffusion model. Like the diffusion model, it predicts the major features observed in unidirectional flows, and the particle phase stresses needed in the suspension balance model can, in principle, be determined from independent rheological experiments, though these measurements are not easily performed. The model has been used to successfully predict migration in a range of flow fields.

Here, the purpose is to provide data regarding the migration of non-spherical particles that can be compared with models and simulations in the future. Only a few studies currently exist for the collective dynamics of concentrated suspensions of fibers. Mondy *et al.* [10] used nuclear magnetic resonance imaging to measure the spatial distribution of rigid rods in a Couette flow. They reported shear induced migration for rod-shaped particles with aspect ratios ranging from 2 to 18 and for volume fractions of 0.3 to 0.4 in Couette flow, where the rod migrated from regions of higher shear rate near the walls of the cell towards the region of low shear rate closer to the inner rotating cylinder of the cell. Overall, it was concluded that the aspect ratio of the fibers played little or no role in the extent of the migration and was also the same as that of spheres.

Along with the center-of-mass positions, the orientation of fibers are also expected to be irreversible. There have been no measurements of the effect of migration on the

orientation distribution, but irreversible changes in orientation distributions have been measured in shearing flows. Studies by Pine *et al.* [85] indicated that, for an oscillatory shear, the orientation distribution could be controlled by varying the amplitude of the strain. For large amplitudes, the fibers align with the direction of the flow, which resembled results in a steady shear [32]; for small amplitudes, the orientation distribution did not vary significantly from its initial state. However, for intermediate strain amplitudes, the fibers preferred to align in the vorticity direction, perpendicular to the flow-gradient plane. Simulations performed by Snook *et al.* [11] addressed the origin of this preferred vorticity alignment and attributed it to short-range interactions between the particles. This study also showed that the alignment depended strongly on the confinement of the cell in the gradient direction between the bounding walls.

Here we use optical imaging techniques to provide observations of demixing of fibers in pressure-driven flows. Results presented in this chapter also relate the orientation of the fibers to their center-of-mass positions. To the best of our knowledge at the time of this work, no measurements have been made for shear induced migration, or the orientation distributions, of rod-shaped particles in pipe-flows. The methods are described in the next section, which is followed by the results.

## 3.1 Experiments

The objective of the experiments presented here is to investigate the dynamics of shear induced migration of rod shaped particles in suspension. Experiments are conducted in an oscillatory pressure-driven flow and particle migration can be quantified using image analyses. These experiments enable the characterization of the microstructure of the suspension as a function of the strain by quantifying not only the distribution of the center of mass position of the fibers, but also the orientation distribution, which is an area that has been largely unresolved. The time-dependent dynamics of this phenomenon is also investigated. The subsections below briefly describe the particle

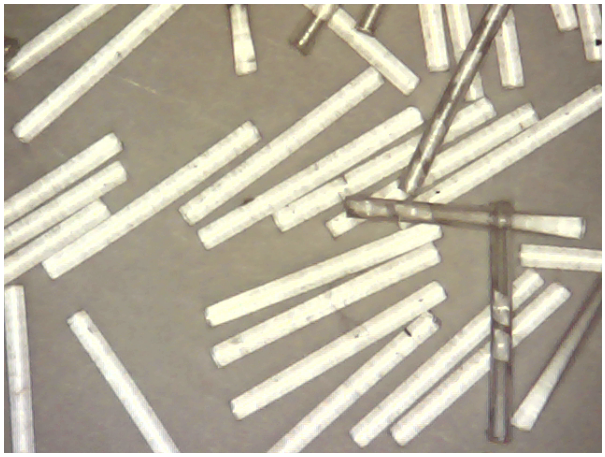

Figure 3-1. Sample photograph for PMMA core fiber optic fibers, stripped using dimethyl sulfoxide (DMSO) and cut using a custom-built guillotine cutting device at Aix-Marseille Université to the desired lengths. The cut edges introduced surface imperfections leading to diffraction of the laser sheet during experiment runs.

and fluid system used, the experimental apparatus, experimental procedure, and image analysis processes. Various results have been described and discussed in Section 3.3.

### 3.1.1 Particles and Fluid

Fiber optic cables with a Poly(methyl methacrylate) (PMMA) core were chemically stripped of their outer fluorocarbon coating by soaking fiber optic filaments in Dimethyl sulfoxide (DMSO) and mechanically wiping off the coating. The stripped cables were mechanically cut into rods of the desired lengths. An example photograph of the stripped and cut fibers is shown in Figure 3-1. The two aspect ratios for our experiments were selected by using the same length, $L = 5.2 \pm 0.2$ mm, and using two diameters, $d = 0.46 \pm 0.06$ and $0.23 \pm 0.02$ mm. The aspect ratio used for these experiments were $A = 11.3 \pm 1.6$ and $22.6 \pm 2.3$, for the two diameters, respectively.

The fluid used for these experiments is similar to the one used for the rheology experiments described in Section 2.1. It is a tri-component mixture of Triton X-100 (73.28%), distilled water (10.72%), and zinc chloride, $ZnCl_2$ (16%). The Triton and water control the viscosity and the refractive index, and the salt controls the density of the fluid. The weight fractions of the components of the suspending fluid are chosen to

match the density and refractive index of the suspended particles. A small amount of Rhodamine 6G dye was added at a concentration of $9 \times 10^{-7}$gm/cm$^3$ to enable contrast imaging with the laser-camera system as shown in Figure 2-1.

Care was taken while preparing the suspensions to prevent trapping air in the viscous fluid. Masses of the particles and fluid were measured to obtain the desired volume fraction for a particular series of experiment runs. The required mass of fibers were first gradually added to the surface of the fluid. This is done, because any forced immersion of particles traps unwanted air. Once the fibers are added, the suspension is then mixed by gently rotating the beaker at an angle. This further reduces the amount of air trapped in the suspension.

### 3.1.2 Experimental Apparatus

The experimental setup, previously used to study the collective motion of spheres [73], was used to observe the change in the microstructure of rod shaped particle suspensions, as well as observe shear induced particle migration in an oscillatory tube flow, and is shown in Figure 3-2. The suspension was loaded into an acrylic tube of length 46.8 cm and of circular cross-section with diameter $2R = 1.65$ cm. For the fibers of length $L$ used in this study, the geometric ratio, $R/L \approx 3.17$. The tube is oriented vertically and a mesh screen is placed at the top and bottom ends of the tube. The small mesh size ensures a constant particle volume fraction within the testing section, as the particles cannot pass through.

The suspension is oscillated by a syringe pump, microcontroller, syringe, and hoses connected to the inlet of the glass tube. Two microswitch triggers are mounted alongside the syringe pump to control the stroke length of each oscillation. The distance between the triggers can be manually adjusted to impose different stroke lengths. The oscillatory strain was in the form of a square wave rather than a sinusoidal one. The rate

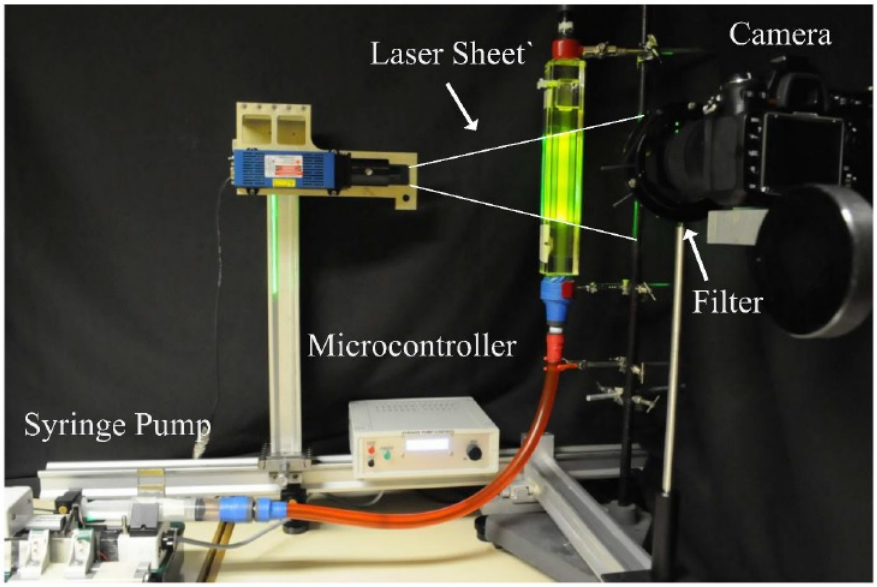


Figure 3-2. Experimental setup to study migration of suspended particles in pipe-flows. A syringe pump is used to create a large amplitude oscillatory flow. The laser sheet and camera system are controlled via a microcontroller for fixed interval exposures. Images captured using this system will be used to track individual particles.

of volumetric displacement $Q(t)$, as a function of time $t$, can be given as

$$Q(t) = (\gamma_0 R)(\pi R^2)\frac{\omega cos(\omega t)}{|cos(\omega t)|}, \tag{3–1}$$

where the $|\cdot|$ indicates the absolute value, for a frequency $\omega$ chosen for values which maintained a low value of the particle Reynolds number, of $O(10^{-3})$ and the Péclet number of $O(10^9)$. The strain amplitude, $\gamma_0$, was chosen to minimize possible end effects while being sufficiently larger when compared to the fiber lengths. The diameter of the syringe used in our experiments, $R_s$ was larger than the tube radius, $R$. To correctly set the distance between the micro-triggers and hence obtain the appropriate strain amplitude, $\gamma_0$, a stroke length, $s$ was set as $\gamma_0 = sR_s^2/2R^3$.

The glass tube is housed within a rectangular plexiglas jacket. The interstitial space between the walls of the jacket and the glass tube is filled with suspending fluid that contains no dye. The purpose of this jacket filled with the fluid is to eliminate the optical distortion caused by the curvature of the tube. A Coherent Lasiris Green PowerLine

Table 3-1. Concentration, $n_{bulk}$, expressed volume fraction, $\phi$, for aspect ratio, A=11.3 and 22.6.

| A | $n_{bulk}$ | $\phi$ (%) |
|---|---|---|
| 11.3 | 0.84 | 5.5 |
| | 1.68 | 11 |
| | 2 | 13.09 |
| | 3 | 19.63 |
| 22.6 | 0.84 | 2.75 |
| | 1.68 | 5.5 |

Laser with a wavelength of 532 nm is used to fluoresce the dyed fluid. The laser passes through a darkened PMMA mask with a slit of 250 $\mu$m cut into it. The mask and the slit were positioned so the laser sheet was only applied to the center of the tube. Since it is the fluid that is dyed and not the particles, the laser fluoresces the suspending fluid and the particles appear dark, creating a contrast which can be imaged. A red long pass filter of 590 nm was used to enhance the contrast of the fluoresced suspension. The camera used for imaging these experiments was a Nikon D300s with an AF-S Micro Nikkor 60mm f/2.8G ED lens. To prevent photobleaching caused by long exposure of the laser, a shutter is mounted in front of the laser. The shutter and the camera were controlled by the microcontroller and the triggers.

### 3.1.3 Experimental Procedure

The fluid containing the fibers was gently remixed and added to the inner circular tube. Before the start of each experiment, the suspension was mixed in the tube using a wire with impellers at different heights. The suspension was then allowed to stand to allow any trapped air to escape from the top of the tube. The volume fraction, $\phi$ corresponding to these concentrations for the two aspect ratios, $A$, can be calculated as $\phi = (n_{bulk})\pi/4A$, and are shown in Table 3-1. The stroke length was set by adjusting the distance between the microswitch triggers to obtain the chosen amplitude of oscillation (either 3.5, 6.5, or 15). For each oscillation, 40 images were taken with a one second interval. Camera settings were chosen to account for the near-zero light conditions and

to capture clear images of the suspension in motion. This was done by maximizing the shutter speed and reducing the aperture size and ISO. A smaller aperture is chosen to limit the depth of field within the glass tube, to only image the particles inside the laser sheet. For the purpose of statistical rigor, at least 2-3 runs of each experiment were performed. From the images obtained from these experiments, we can ascertain the microstructure of the suspension as a function of imposed flow parameters by measuring the spatial and orientation distributions using particle tracking velocimetry and image analyses techniques.

## 3.2 Image Analyses

A brief schematic of the image analyses processes are shown in Figure 3-3. Positions of the centers of mass and the orientations can be calculated from the images obtained from the experiments. By measuring the particle volume fraction across the tube, we can examine demixing of the suspension. The experimental images were processed, using multiple steps to clean the image as shown in Figure 3-3 (a), and analyzed to determine if there was a migration of the fibers.

A cropped image is used for the data analysis and shown in Figure 3-3 (b). We use the ”skimage” analysis package available through a standard Python distribution. One of the primary objectives is to calculate the areal fraction and the spatial distribution of the particles across the radial coordinate of the tube. The image quality is questionable in the second half of the image; the mechanical cutting of the fibers refracts the laser sheet and creates streaks generally found in the half of the image furthest from the laser sheet. Therefore, only the initial half of the images are used in the image processing.For the local adaptive contrast enhancement, shown in Figure 3-3 (b), equalize_adapthist was used, which is a subfunction of the exposure library in the skimage package. This algorithm uses histograms computed over a user-specified number of ”bins” which determine the contrast resolution of the treated image. The number of bins determines the spacing of the domains and help increase the contrast between the particles and the

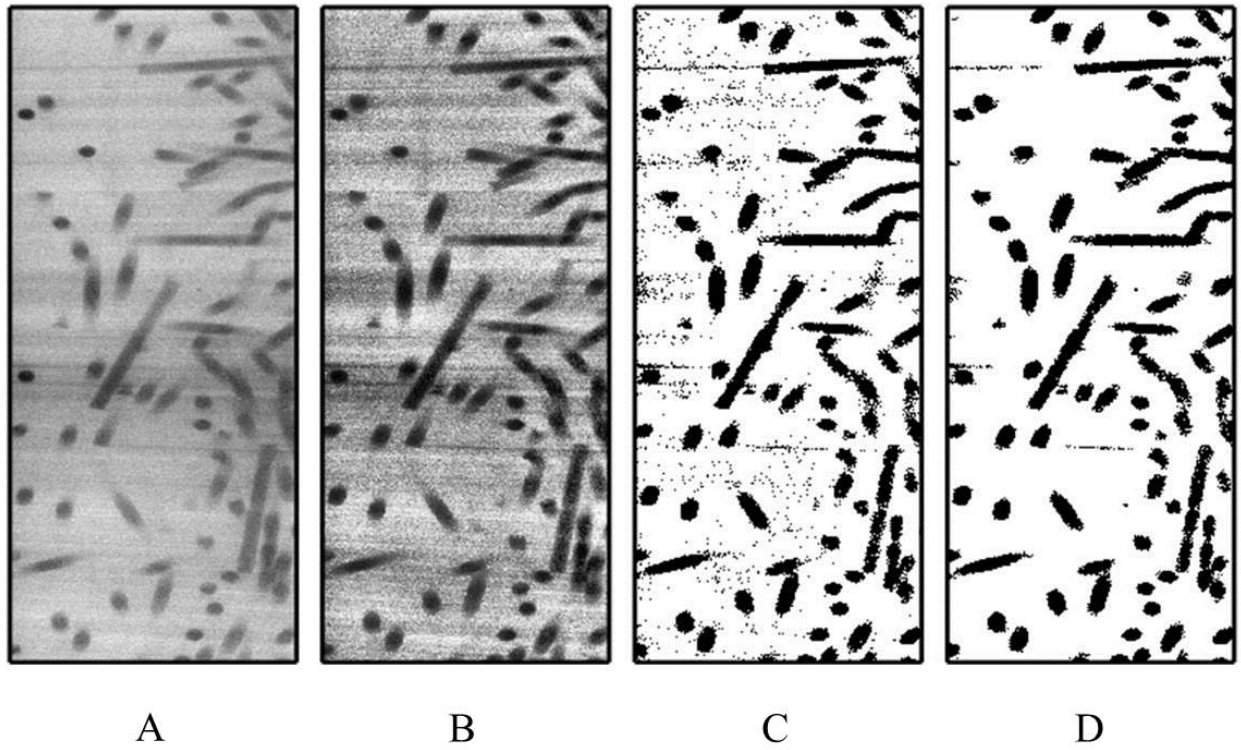


Figure 3-3. Example schematic showing the various image processing techniques for a sample image of bulk concentration, $n_{bulk}$ = 0.84. A) The raw image cropped to size; B) adaptive equalization and C) thresholding where the reference block size for the process is user-defined; D) the cleaned image after the removal some of the noisy pixels to give a better binary image which can be analyzed using particle tracking techniques.

background. The contrast image was then run through an adaptive threshold function threshold_local which is part of the filters library, shown in Figure 3-3 (c). This step is also known as adaptive or dynamic thresholding in older versions of Python. Adaptive or local thresholding is a weighted mean determined by the neighboring pixels subtracted by the constant offset defined. The offset for this function has a dramatic effect on the treated image and is hence user-defined for images from each experimental run. The method for thresholding used was Gaussian which is the default method. The result thresholded image was of enhanced contrast and every pixel above the threshold value was considered to be part of the foreground. However, because of the non-spherical shape of the particles, it was still difficult to distinguish the particles from

residual noise caused due to diffraction or shadows caused by surface imperfections. To obtain images of higher clarity, the final step of the image analysis process was the remove_small_objects which is part of the morphology library, shown in Figure 3-3 (d). This function removes connected pixels smaller than a defined size. The result of the image analysis processes is a binary image of dark pixels which indicate the fiber on a white background which is the suspending fluid.

As a test of the validity of the treatment process, the areal fraction was calculated from the treated image and compared to the known volume fraction of the particles in the tube for any run. Ideally, the treatment would have removed all noise from the images, leaving only the fibers, and would roughly the same area fraction as the initial volume fraction. The treatment parameters were adjusted to help minimize the difference between the calculated areal fraction of the images and the known volume fraction of the suspension. A large subset of each cycle was averaged to create a distribution of the area fractions. A radial weighting was applied to find the average and error of the area fraction across the diameter of the tube. This radial weighting can be given as

$$\Phi = \frac{\int_0^R \phi(r) r dr}{\int_0^R r dr} = \frac{\sum_1^N \phi(r_i)\left(\frac{r_{i+1/2}^2}{2} - \frac{r_{i-1/2}^2}{2}\right)}{R^2/2}, \tag{3–2}$$

where, $\phi(r_i)$ is the volume fraction to be calculated which is a function of the radial position $r$ across a user-set calculation index $i$. The distance between the centerline and the wall of the tube, $R$, is half the size of the frame.

### 3.3 Results and Discussion

The goal of the experiments was to examine the key parameters that control shear induced migration in fiber suspensions. Figure 3-4 shows a representative set of processed images for an experiment with fibers of aspect ratio $A \approx 11$ at a particle concentration of $n_{bulk}$ =0.84 in an oscillatory pressure driven flow at the strain amplitude $\gamma_0$ = 15. This figure shows the evolution of the distribution of the fibers in the tube flow to qualitatively illustrate the existence of shear induced migration. Here, the initial uniform

distribution is defined where the accumulated strain, $\gamma$ = 0. It is important to note that only half of the image, the one closer to the laser, was used for the analyses. This is because the image quality severely deteriorated as we moved away from the laser.

Each panel in Figure 3-4 is a snapshot of the suspension at the end of a oscillation cycle. For example, the panel at an accumulated strain $\gamma$ = 300 at $\gamma_0$ = 15 corresponds to the structure of the suspension at the end of the twentieth oscillation. The data is presented as a function of the accumulated strain as it is a more convenient way of comparing the extent and rate of migration for experiments at different amplitudes, which differed in their number of oscillations.

As the suspension is oscillated, the isotropic initial distribution demixes, as can be seen in intermediate images, which in the case of Figure 3-4 is at $\gamma$ = 300 and 600, respectively. At a sufficiently large accumulated strain, for example, at $\gamma$ = 900, the microstructure does not significantly change as the strain increases. This structure shows a distribution which is more concentrated at the center of the tube, at $r/R = 0$ and less concentrated near the walls at $r/R = 1$, showing direct qualitative evidence of shear induced migration of the suspension under these conditions.

Processed sets of images like the one shown in Figure 3-4 can be used to calculate local particle concentrations, which can be used to quantify the migration phenomenon and is described in detail in Subsection 3.3.1. Additionally, these processed images can be used to quantify the orientation distribution of the fibers in these experiments. A detailed study of the orientation distribution, and the effect of migration on the orientation distribution is described in Subsection 3.3.3.

### 3.3.1 Areal Fraction Distribution

Intensity data were extracted from the processed images, where the dark pixels correspond to the fibers against the bright background which is the suspending fluid. To generate quantitative information regarding the local particle concentration as a function of radial position and strain, the fraction of pixels filled by a particle (i.e. black)

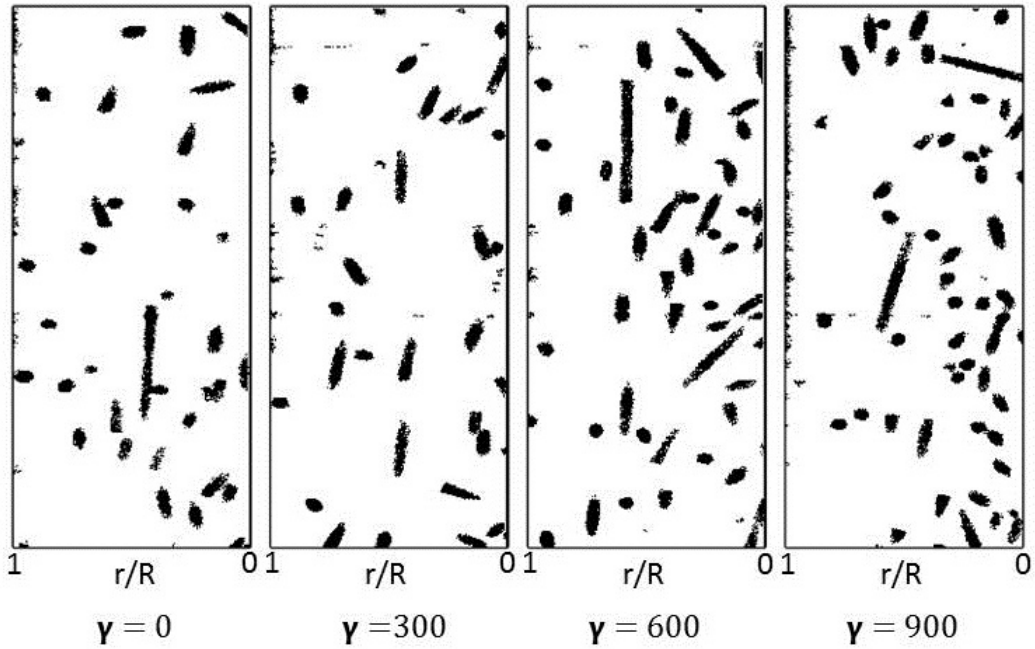


Figure 3-4. Set of processed images that qualitatively illustrate shear induced migration in concentrated fiber suspensions. The fiber concentration is $n_{bulk}$ = 0.84, the strain amplitude $\gamma_0 = 15$, fibers have an aspect ratio $A \approx$ 11.

in each vertical row of pixels in the images was recorded. The overall number density at a volume fraction, $\phi(r)$, is given by $4A\phi(r)/\pi$.

The areal fraction data was averaged over at least three experimental runs to reduce fluctuations in the runs. One such averaged areal distribution, corresponding to the case described in Figure 3-4 is shown in Figure 3-5. It can be seen that as the accumulated strain increases, the local areal fraction increases at the center of the channel, at $r/R$ = 0, and decreases near the wall. This is in accordance with the qualitative observation shown in Figure 3-4. It is important to note here that the areal fraction distribution describes the average number of particles in the pixel-width frame, and hence the bulk concentration $n_{bulk}$ is conserved. The error associated with the calculation of the average local areal fraction is within 10%. For example, for an initial bulk concentration $n_{bulk}$ = 0.84, the calculated bulk concentration from the processed images is 0.83 $\pm$ 0.04 at $\gamma$ = 0 for the representative case described in Figure 3-5. This

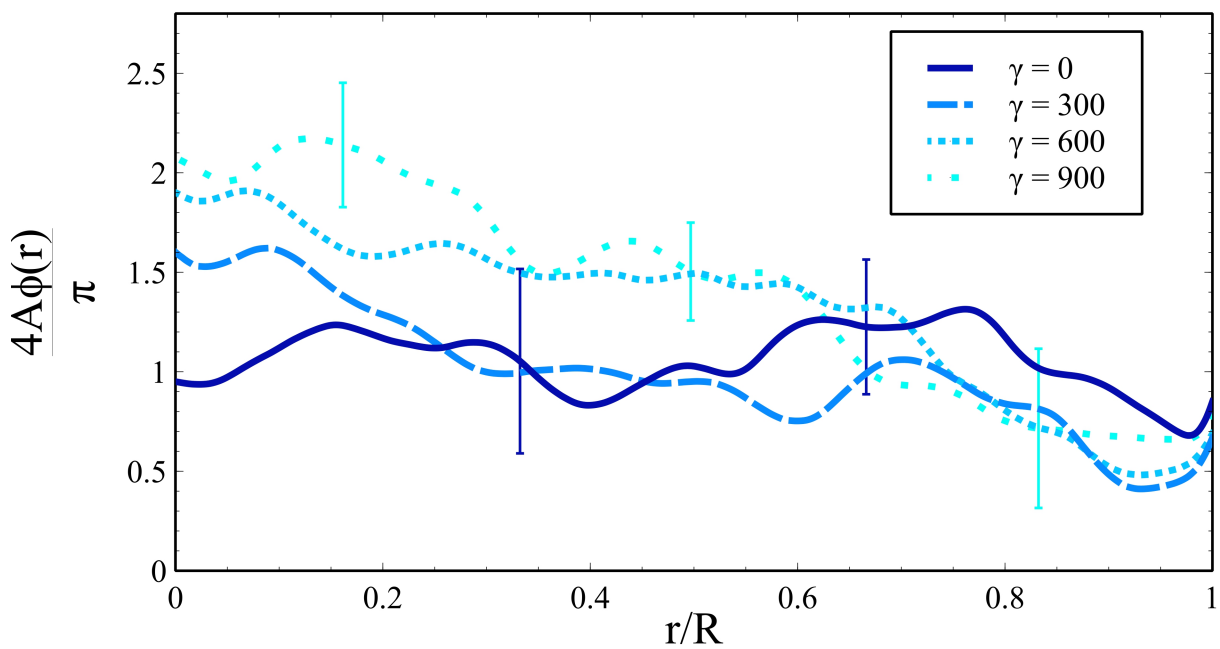


Figure 3-5. For initial bulk concentration $n_{bulk}$ = 0.84, $\gamma_0$ = 15, and $A \approx$ 11, the local number density, $4A\phi(r)/\pi$, is plotted as a function of the radial position, $r/R$, of the tube of radius $R$ for different accumulated strains. Shear induced migration can be observed as the accumulated strain increases towards $\gamma$ = 900. Individual curves for the different strains correspond to the example panels shown in Figure 3-4

is the first quantitative claim of shear induced migration for fiber suspensions at these conditions in an oscillatory pipe flow.

To identify the effect of strain amplitude on the observation of migration, experiments were performed for strain amplitudes $\gamma_0$ = 3.5 and 6, in addition to the case of $\gamma_0$ = 15 shown in Figure 3-5. Shear induced migration was observed for all of the above-mentioned conditions. The dependence of strain amplitude is shown in Figure 3-6 to the sample case shown in Figure 3-5. It can be seen that the strain amplitude has an effect on the areal fraction distribution. At the same concentration, accumulated strain, and aspect ratio, the areal fraction near the center of the tube increased with a higher strain amplitude. This difference in results can be attributed to the rearrangement of the microstructure with the flow. The reversal of flow at different points, corresponding to the different strain amplitudes alters the microstructure to different extents. For example,

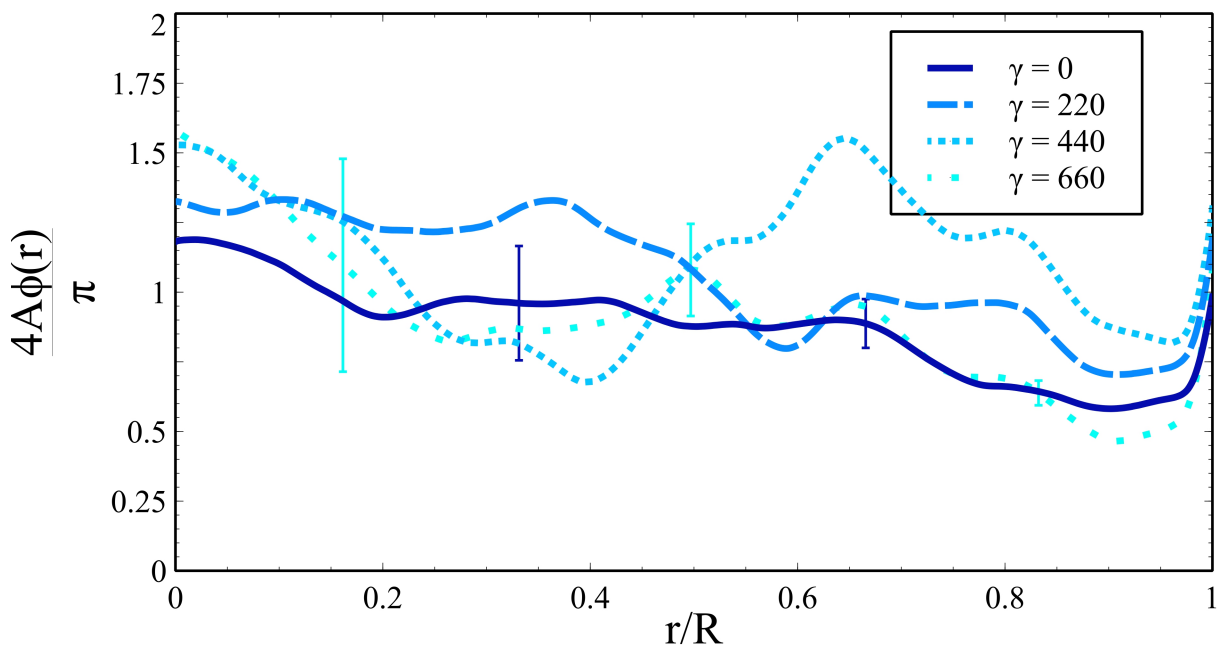


Figure 3-6. The dependence of the strain amplitude on migration is shown by looking at the local number density, $4A\phi(r)/\pi$, for experiments with the same fiber aspect ratio $A \approx 11$, $n_{bulk}$ = 0.84, but for a different strain amplitude, $\gamma_0$ = 6 as compared to Figure 3-5 where $\gamma_0$ = 15.

for flow at steady state, defined as the state at which the microstructure has become steady, if the flow is reversed, there is a finite strain required for the steady microstructure to develop again. This phenomena is not surprising and it has been studied for the case of spheres [86], and it was concluded that at least four to six strain cycles were required to reclaim the steady microstructure, and this rate depended on the volume fraction. Hence we would not necessarily expect results for our rod experiments to be the same, as many cycles (beyond the range of our experiments) may be required for the rods to return to their steady microstructure.

In contrast, a higher aspect ratio did not show a change in the migration behavior, as shown in Figure 3-7. Note that the length of the fiber was kept constant for the two aspect ratios. This means that particle concentration $nL^2d$, and not the volume fraction $\phi$ is the appropriate parameter to quantify migration in our experiments.

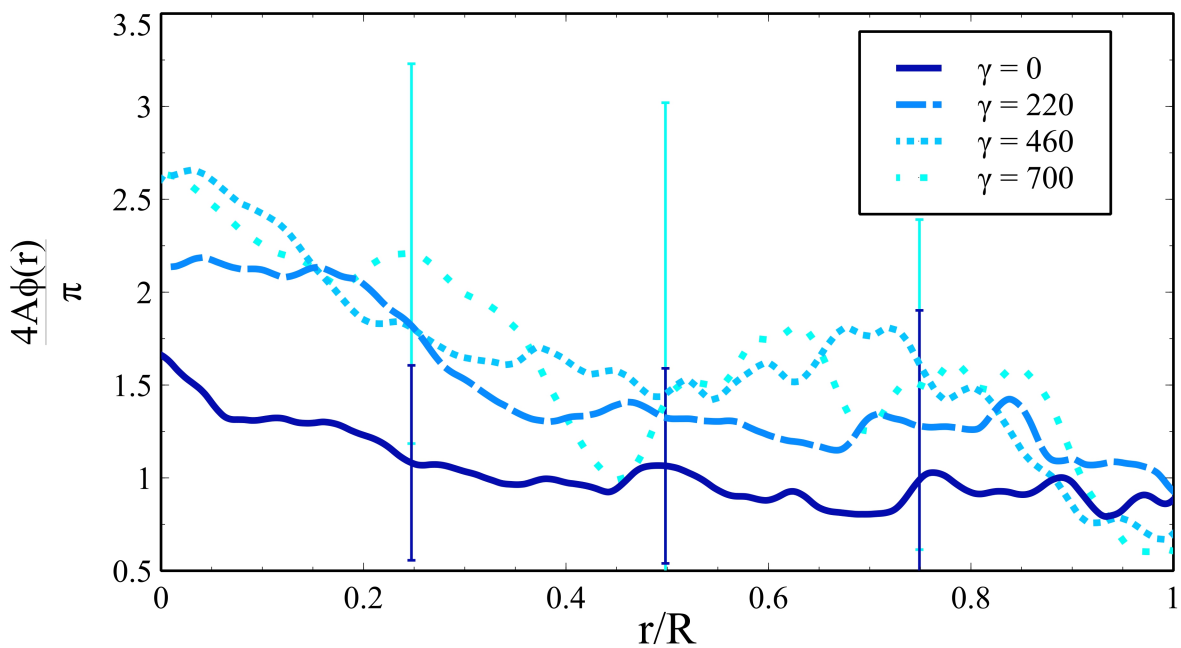


Figure 3-7. For a bulk initial concentration $n_{bulk}$ = 0.84, $\gamma_0$ = 15, and aspect ratio $A$ = 22.6, the dependence of the fiber aspect ratio by comparing local number density as compared to Figure 3-5 for identical conditions but for fibers having an aspect ratio $A$ = 11.3.

However, experiments were conducted, where no significant migration was seen by observing the evolution of the areal fraction distribution as shown in Figure 3-8. Figure 3-8 (a) shows that at a low concentration, at $n_{bulk}$ = 0.5, for an aspect ratio $A \approx 11$, and $\gamma_0$ = 15, the distribution after an accumulated strain of 720 is not significantly different from the initial distribution indicating that there is no significant migration. There are two proposed reasons for the lack of observable migration at these conditions. Firstly, the concentration is too low for a significant number of particle interactions to occur. A low number of particle contacts leads to a low particle normal stress which could account for the lack of observable migration. Secondly, for a lower concentration, the strain required for a fully developed microstructure is much higher and may be beyond the range of strain that is measured in our experiments. Migration does not occur at low strain amplitude $\gamma_0$ as the displacement per cycle is insufficient to disturb the initial microstructure, and hence no migration occurs. At higher concentrations as shown

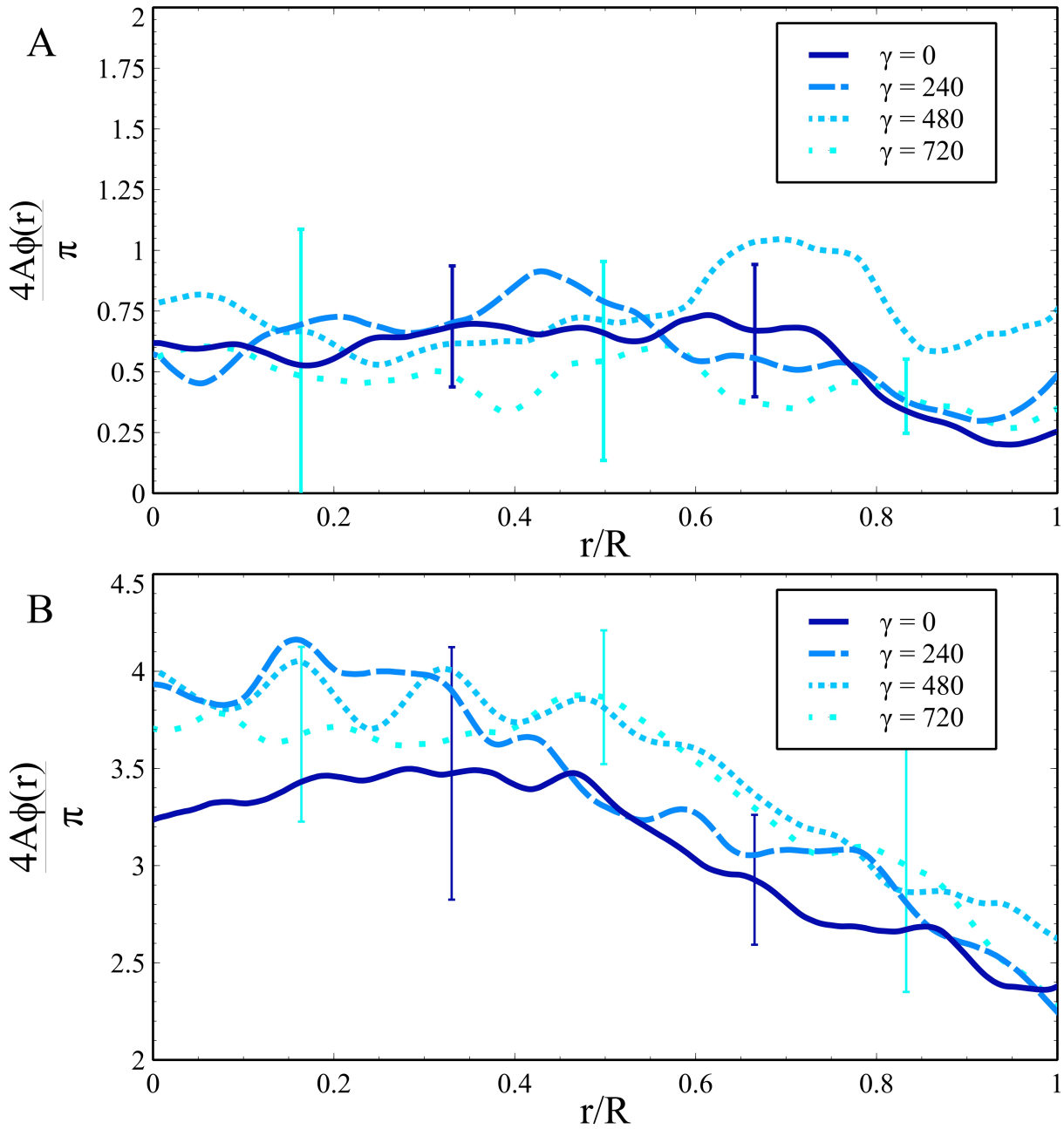


Figure 3-8. For $A \approx 11$ and $\gamma_0$ = 15, no significant migration was seen for A) $n_{bulk}$ = 0.5 and B) $n_{bulk}$ = 3.

in Figure 3-8 (b), the effects of confinement hinder any collective motion of the fibers. Although, more investigation into higher concentrations is required.

Figure 3-10 plots the extent of migration for all conditions tested to enable a comprehensive comparison. For the purpose of calculating the extent of migration two

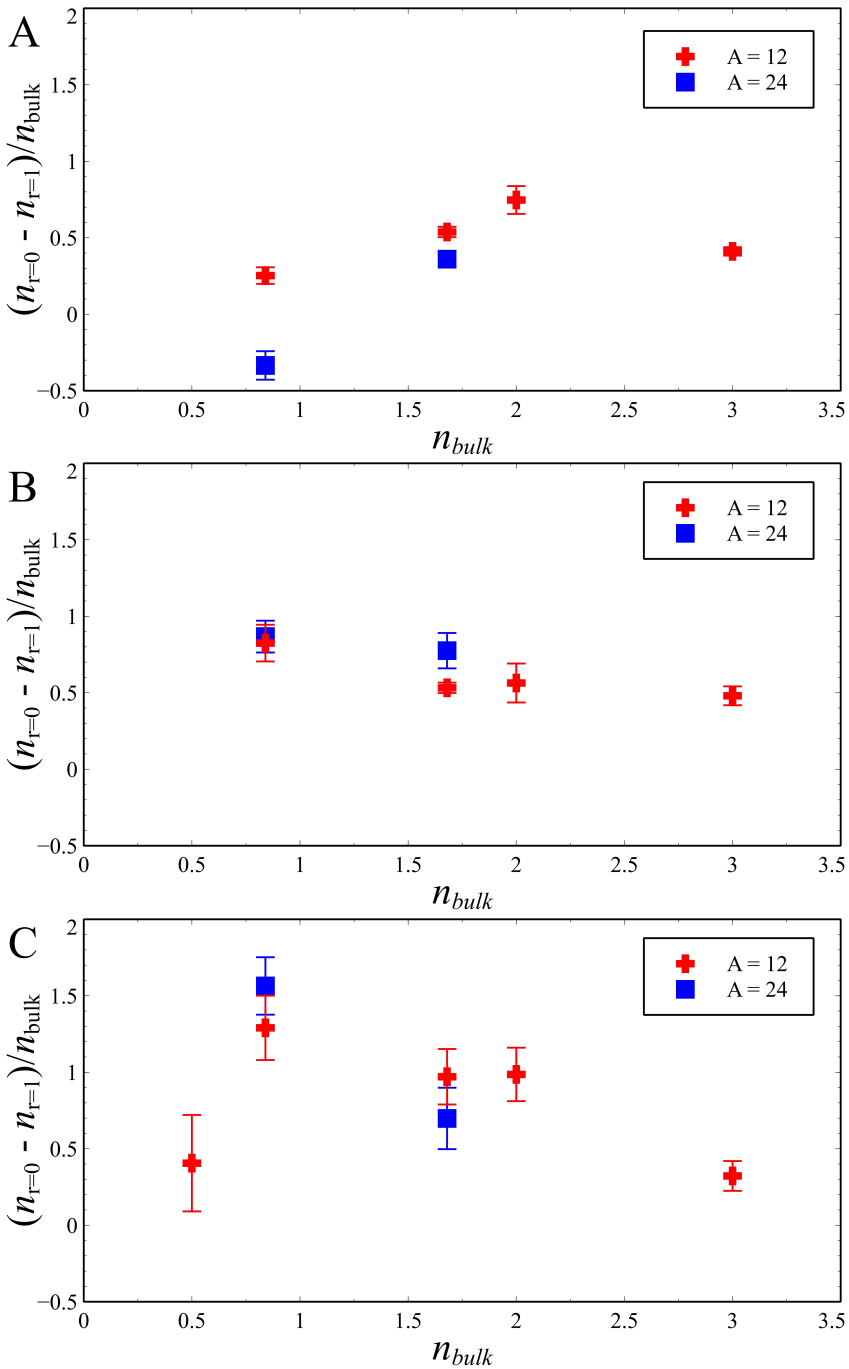


Figure 3-9. Extent of migration as a function of the bulk particle concentration, $n_{bulk}$, A) For a strain amplitude $\gamma_0$ = 3.5, B) $\gamma_0$ = 6, and C) $\gamma_0$ = 15, for aspect ratio, $A$ =11.3 (red), and $A$ = 22.6 (blue).

bins were chosen, corresponding to $1/16^{th}$ the width of the frame, near the center and the wall of the tube . The extent of migration was calculated as $(n_{r=0} - n_{r=1})/n_{bulk}$, where $n_{r=0}$ is the areal fraction at steady state at the center of the tube ($r/R$ =0), and $n_{r=1}$ is the steady state areal fraction at the wall of the tube , where $r/R$=1, and $n_{bulk}$ is the averaged areal fraction across the tube at the largest available strain. Note that the value of $n_{bulk}$ is radially weighted. Figure 3-9 shows the dependence of the extent of migration with particle concentration for different strain amplitudes, for the two aspect ratios. An important result is that maximum extent of migration was observed at $n_{bulk}$ = 0.84, independent of both amplitude and aspect ratio. According to the results presented in Figure 3-9, the peak extent of migration was seen for suspensions of concentration $n_{bulk}$ = 0.84, strain amplitude $\gamma_0$ = 15, for fiber aspect ratio $A \approx$ 23. As the concentration is increased, the extent of migration decreases. These results are corroborated by the results shown in Figure 3-5 which showed large observed migration, and 3-8 (a) and (b) which showed a significantly lower extent for cases at low ($n_{bulk}$ = 0.5) and high ($n_{bulk}$ = 3) concentrations, respectively.

### 3.3.2 Dynamics of shear induced migration

One of the major questions to be answered is whether the measurements shown in Figure 3-9 are at steady state. The dynamics of the migration are evaluated by observing the extent of migration as a function of the accumulated strain as shown in Figure 3-10. As seen in the figure, the claim that the system has reached steady state is a complex one. This is due to the large fluctuations in the measurements of the extent of migration, caused due to the fluctuations in the motion of the fluid and fibers themselves. One of the proposed methods to smooth the harsh fluctuations is to move away from the discrete method of evaluating the extent of migration and move towards an integral approach. One such approach is to define an equivalent radius $r_e$, where the bulk areal fraction at $r < r_e$, is equal to the volume fraction over $r_e < r < R$. The volume fractions are radially weighted using Equation 3–2 at $r_e$ and $R - r_e$. The extent of migration can

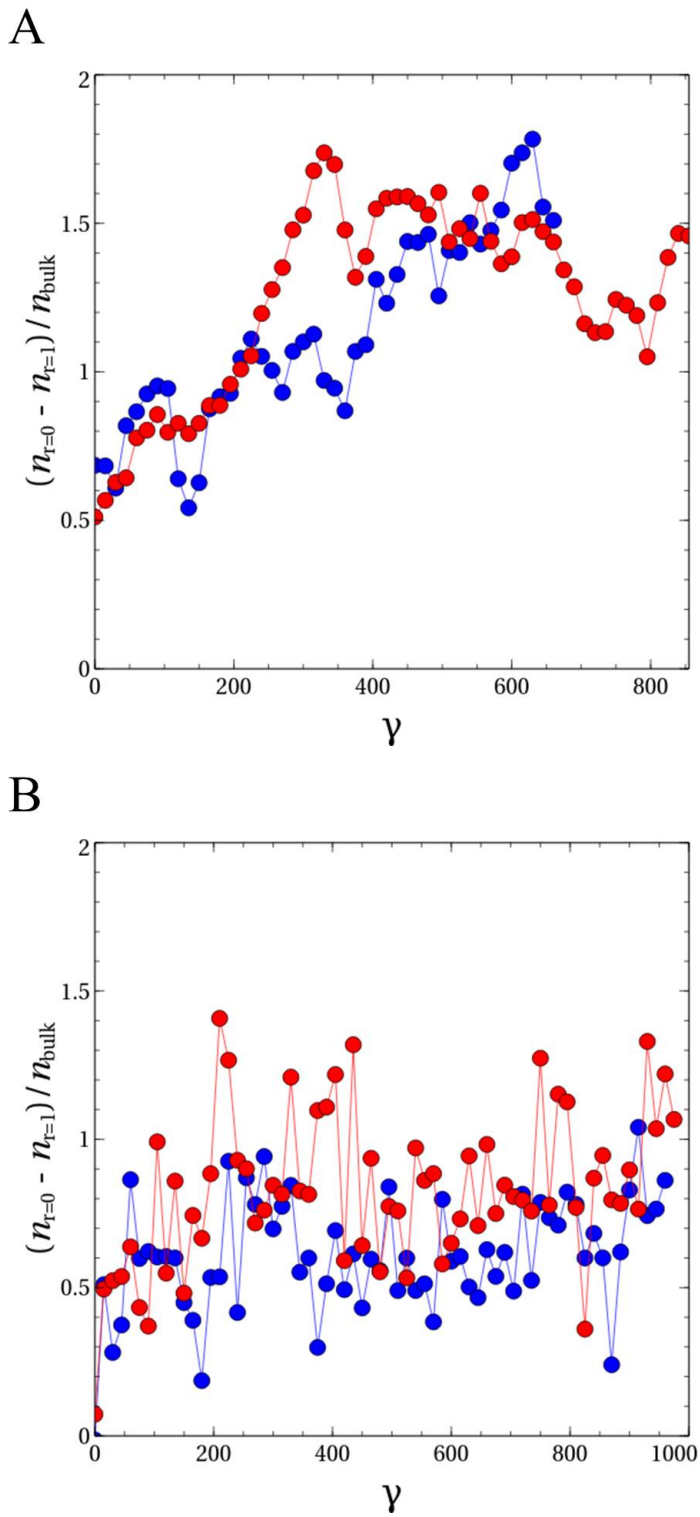


Figure 3-10. Evaluation of steady state can be performed by observing the extent of migration as the accumulated strain $\gamma$ is increased for $A$ = 11.3 (red) and 22.6 (blue), and $\gamma_0$ = 15, for A) $n_{bulk}$ = 0.84 and B) $n_{bulk}$ = 1.68.

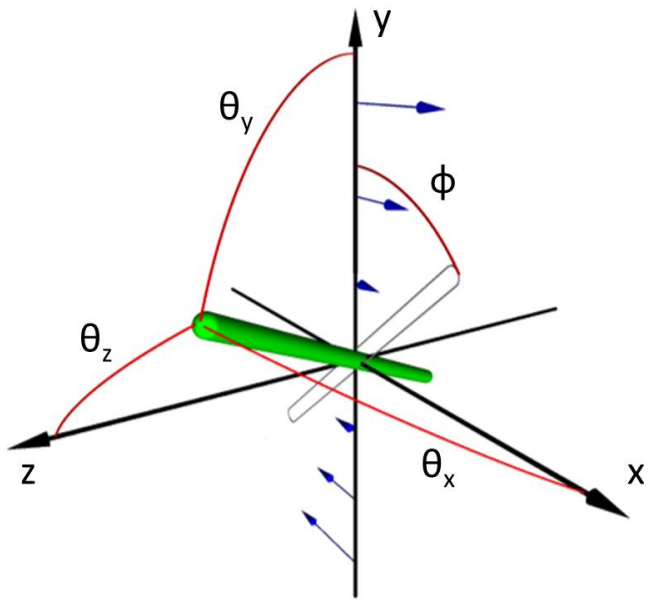


Figure 3-11. For a shearing flow in the x-direction having a gradient in the y-direction, the orientation can be quantified using the angle $\phi$ which is the angle made with respect to the gradient direction using the projection of the rod in the flow-gradient plane, and $\theta_z$ which is the angle made by the fiber and the vorticity or the z-direction.

now be expressed as a measure of $r_e$ lower than $R/2$, as there are more fibers near the center than towards the wall. This approach for analyzing the extent of migration has not yet been performed.

### 3.3.3 Orientation distribution

Details about the orientation distribution can also be extracted using the processed images. For the purpose of this work, the orientation of a fiber is quantified by measuring the angle $\theta_z$, the angle made by the rod and the vorticity direction, and $\phi$, which is the angle that the projection of the rod makes with the flow-gradient plane with respect to the gradient direction, as shown in Figure 3-11.

The probability distribution, $P(\theta_z)$ as a function of the angle $\theta_z$ is shown in Figure 3-12. The processed image was divided into three equal bins, and the average probability distribution was plotted, as shown in Figure 3-12. According to the definition of the orientation shown in Figure 3-11, the fiber is oriented in the vorticity direction as $\theta_z \to 0°$.

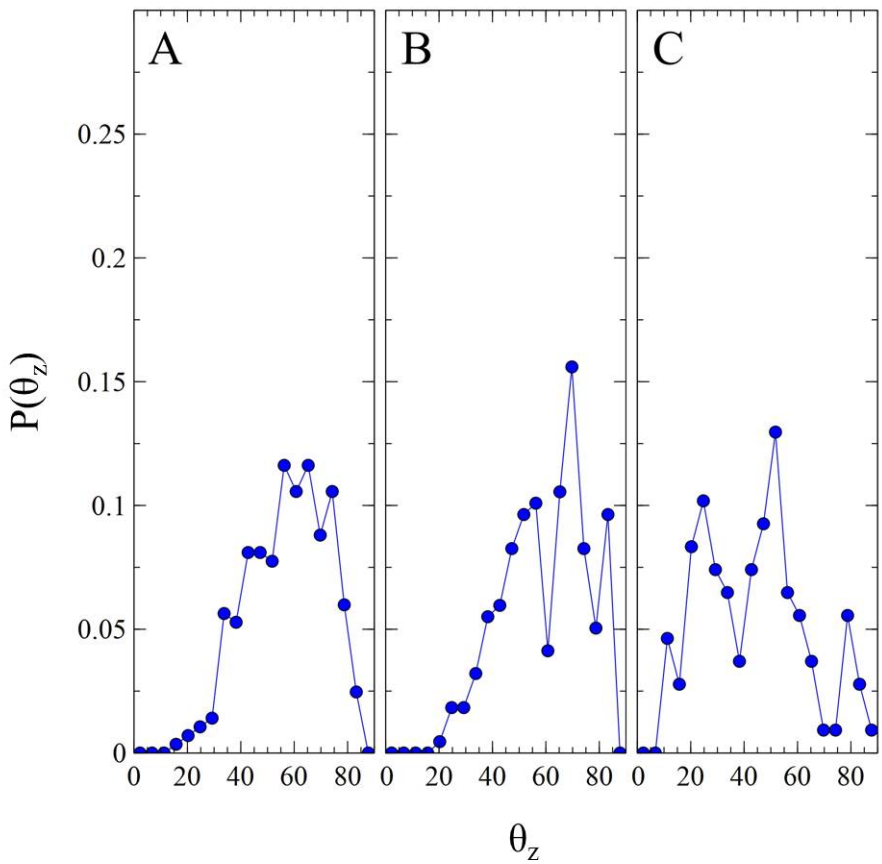


Figure 3-12. For $A \approx 11$, at concentration $n_{bulk}$ = 0.84, and $\gamma_0$ = 15. The probability of finding a rod at angle $\theta_z$, $P(\theta_z)$ decreases as we move towards the center of the tube, as seen by observing the distribution at A) $0 < r < 0.33R$ , B) $0.33R < r < 0.66R$, and C) towards the wall at $0.66R < r < R$. The probability $P(\theta_z)$ of finding a particle at an angle, $\theta_z = 0°$, shows a preferential alignment of the fiber in the vorticity direction, near the walls.

As seen in Figure 3-12, there is negligible vorticity alignment near the center of the tube, at $0 < r < 0.33R$. The probability of vorticity alignment increases for fibers near the walls, at $0.33 < r < 0.66R$. The vorticity alignment observed in these experiments validates the results obtained from numerical simulations performed by Snook *et al.* [11], and experimental results of rod suspensions in a Couette flow [85].

To begin analyzing $\phi$, it is important to neglect all fibers that are closely oriented with the vorticity direction. The angle $\phi$ cannot be measured for these fibers. Fibers that are oriented perpendicular to the flow-gradient plane, and hence the laser sheet

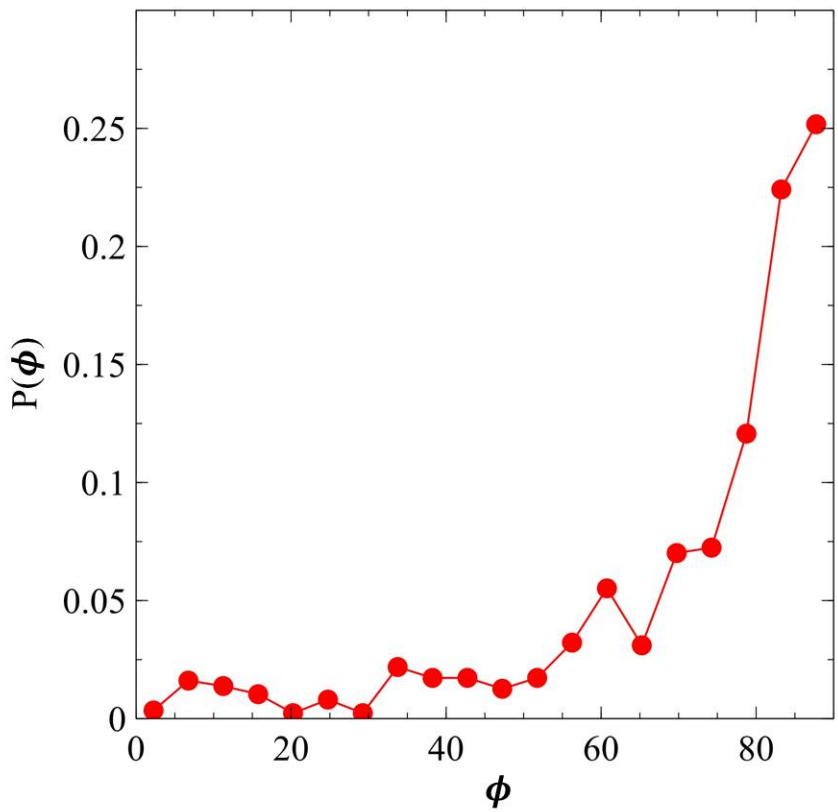


Figure 3-13. For $A \approx 11$ at bulk initial concentration $n_{bulk}$ = 0.84, and $\gamma_0$ = 15, the probability $P(\phi)$ of finding a particle at an angle $\phi$ shows a preferential alignment for the flow direction, where $\phi$ = 90°.

appear as circles in the 2-D images taken during the experiment runs. These circles and all dark regions below a defined area threshold are neglected during the calculation of $\phi$. Figure 3-13 shows the average probability of finding a particle $P(\phi)$ distribution across the entire frame of the reference case described in Figure 3-4, and Figure 3-14 shows a distribution across the three bins, similar to the analysis of $\theta_z$. As expected, a significantly high $P(\phi)$ was observed for $\phi = 90°$ implying that the fibers show preferential alignment in the flow direction. Negligible probability for $\phi = 0°$ shows an insignificant propensity for fibers to align in the gradient direction.

## 3.4 Conclusions

Direct optical imaging techniques were used to investigate the shear-induced migration of concentrated suspensions of rigid rods in an oscillatory parabolic flow. At

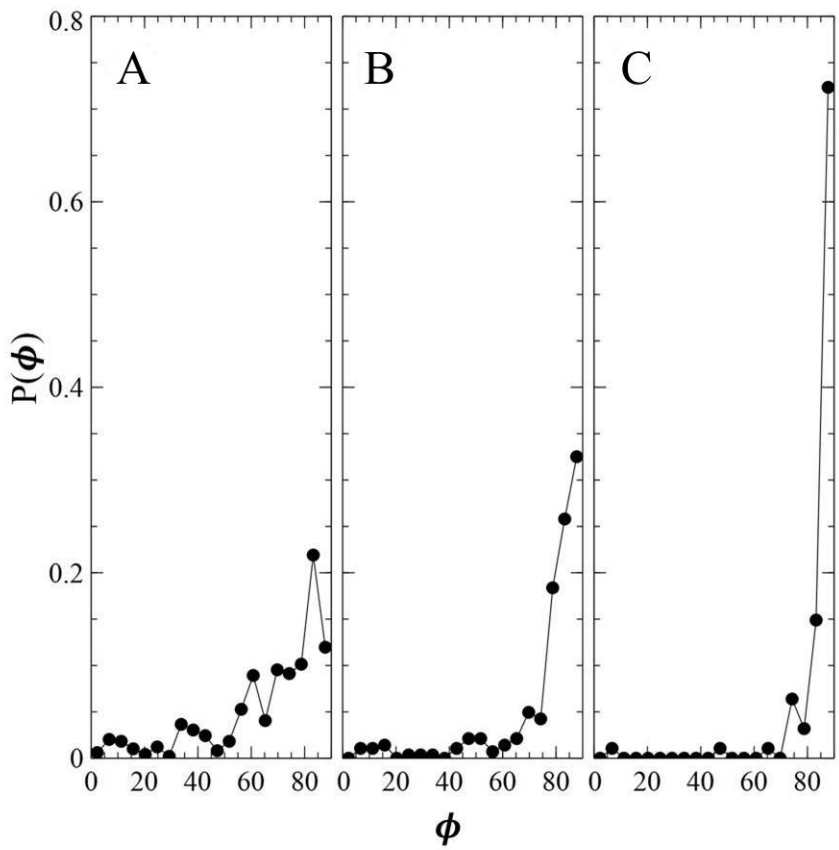


Figure 3-14. For $A \approx 11$, at concentration $n_{bulk}$ = 0.84, and $\gamma_0$ = 15, the probability $P(\phi)$ of finding a particle at an angle $\phi$ shows a preferential alignment for the flow direction, where $\phi$ = 90°. This probability increases as we move from the center of the tube , at A) $0 < r < 0.33R$ , B) $0.33R < r < 0.66R$, and C) towards the wall at $0.66R < r < R$.

the time of this work, the results described in Section 3.3 show the first evidence and detailed measurements of shear-induced migration for non-spherical particles like rigid rods in pressure driven flows. The initial volume fractions used corresponded to an $nL^2d$ = 0.84, 1,68, and 3 for fibers of aspect ratios $A$ = 11.3 and 22.6 respectively. The suspension was oscillated with strain amplitudes $\gamma_0$ = 3.5, 6, and 15. At least three runs were performed for each experimental set for accuracy while calculating average results.

A local particle concentration distribution was presented for a representative case, for fibers of $A \approx 11$, at an initial bulk concentration $n_{bulk}$ = 0.84 oscillated with an amplitude $\gamma_0$ = 15 shown in Figure 3-5. This case was chosen as it exhibited the highest

extent of migration, and was used to investigate the effect of strain amplitude shown in Figure 3-6 and aspect ratio as shown in Figure 3-7. As an important divergence from the behavior of spheres [86], results presented in Figure 3-6 was not independent of the strain amplitude. Hence the results, even at the highest strain amplitude, cannot be assumed to represent those expected in a steady tube flow. The aspect ratio did not play a significant role in affecting the extent of migration.

At low concentrations, for example at $n_{bulk}$ = 0.5, particle interactions were infrequent. Hence no significant migration was observed within the strain limit of our experiments shown in Figure 3-8 (a). In addition, for low amplitudes $\gamma_0$, there is a limit under which the motion of fiber suspensions remains reversible, which further confirmed this observation. Similarly, confinement prevented the collective motion of the fibers at high concentrations, for example at $n_{bulk}$ = 3 as shown in Figure 3-8 (b).

The extent of migration was calculated using a normalized difference between the concentration of the fibers near the walls and the center of the frame. From our results, it was concluded that the extent of migration was highest at $n_{bulk}$ = 0.84, and decreased with further increase in concentration. This limit was independent of strain amplitude and fiber aspect ratio. The extent of migration did not depend on the volume fraction, but the particle concentration $nL^2d$, as the two aspect ratios used had the same lengths but different diameters. To improve the analysis, an integral method for calculating the extent of migration was proposed which would help smooth the fluctuations observed in the data.

The dynamics of rod migration were also investigated by observing the temporal evolution of the extent of migration. Reaching steady state remains a significant challenge to these measurements, as the strain required is large, and there are large fluctuations in the motion of the fibers which increase the variation in the measured areal fractions. It is expected that suspensions with higher fiber concentration would

reach a fully developed microstructure quicker than lower concentrations, and the effect of concentration would be independent of aspect ratio.

Orientation data was also extracted from the processed images. The fiber orientation was quantified using the angle $\phi$ made by the projection of the fiber in the flow-gradient plane, and the $\theta_z$ which is the angle made by the fiber and the vorticity direction. Results obtained from a distribution of the angle $\theta_z$ showed a negligible probability of a fiber aligning in the vorticity direction near the center of the tube, but a high probability of alignment in the vorticity direction near the walls. A probability distribution of $\phi$ indicated strong preference for fibers to align in the flow direction and negligible probability of alignment with the gradient direction.

# CHAPTER 4
# CONCLUSIONS

Concentrated suspensions are seen in nature and have a variety of applications in industry. Previous studies have focused mainly on dilute to semi-dilute suspensions of spherical particles. There has also been significant experimental work and numerical analyses performed on concentrated suspensions of spheres. However, these studies are far from practical industrial examples, which often concern suspensions of particles that are polydisperse in size and shape. For example, elongated particles are added to concrete slurries to increase its mechanical strength [2] and rod-shaped particles are added to drilling fluids to change their rheological properties [4].

In manufacturing processes, there is always a need to transport high solid-content suspensions. Furthermore, there is a significant need for progress in the measurements of rheological properties, modeling, and interpretations of these measurements in concentrated suspensions. The work presented in this dissertation resolves questions regarding more practical suspensions and the results represent a significant improvement in the modeling of rheological relations between the particle volume fraction and stresses, viscosities, friction coefficients etc., that will help predict the dynamics of concentrated suspensions of non-colloidal rigid rods. Accurate measurements and interpretation of rheological data of concentrated suspensions help in the design, performance, and energy consumption of process equipment.

Experiments were run using a novel pressure-imposed rheology techniques using a custom-built rheometer. This technique borrows heavily from the frictional approach to rheology, previously used for dry granular rheology and now adapted to dense suspensions (explained in Appendix C). Results presented in Section 2.2 are the first rheological measurements for non-colloidal rigid rods at particle concentrations near maximum packing fractions. A conspicuous result was the appearance of yield stresses in measured values of both the shear and normal components, which is anomalous for

Newtonian suspensions, as described in Figure 2-5. The origin of these yield stresses remains unknown. However, several possible explanations for the origin of the yield stresses were proposed such as attractive interaction forces and finite-size effects close to the jamming point. Subtracting these yield stresses revealed a viscous scaling for both the shear stresses as well as the particle pressures as seen in Figure 2-4.

We also related the divergence of the rheological parameters to the maximum packing fraction, and proposed relations to model this divergence. This model equation was a function of the maximum packing fraction, $\phi_m$ and is given as

$$\eta_s(\phi) = 14.51 \left( \frac{\phi_m - \phi}{\phi_m} \right)^{-0.90} . \tag{4–1}$$

The exponent given in Equation 4–1 differs to that for spheres as described by Boyer [63], and shown in Figure 2-7. Similarly, a constitutive law for the coefficient of friction was found,

$$\mu(\phi) = \mu_s + \alpha \left( \frac{\phi_m - \phi}{\phi} \right) + \beta \left( \frac{\phi_m - \phi}{\phi} \right)^2 , \tag{4–2}$$

where $\alpha$ and $\beta$ were calculated from fitting the experimental data. The values calculated from Figure 2-7 (c) differed significantly from that of spheres calculated by Dagois-Bohy [64]. In addition, the collapse of our measurements onto a single curve, also shown in Figure 2-7, further confirms our hypothesis that, at high concentrations, short-range lubrication interactions and particle contacts should capture the dynamics accurately, and long-range hydrodynamic interactions could safely be ignored. This conclusion would greatly eases the computational complexity while running simulations of these systems.

Future work regarding the rheology of concentrated fiber suspensions will mainly concern comparing results obtained from the pressure-imposed rheometer to those obtained from numerical simulations. There are limited results from numerical simulations of concentrated suspensions, especially near the limit of jamming. Ongoing work includes simulating feedback loop on one of the bounding walls in response to

the imposed load applied to the suspension, which is similar to the pressure-imposed rheology setup. Initial work is currently focused on suspensions of hard spheres for ease of computations, but future work will include rigid rods. Questions regarding the appearance of yield stresses and the effect of these yield stresses on the bulk rheological measurements can be answered via numerical simulations. In addition, the microstructure at jamming-limit concentrations is largely unresolved. At higher concentrations, suspensions of rigid rods are expected to be aligned in the direction of shear. Figure 2-6 showed the range of aspect ratios and maximum packing fractions recorded in our experiments. Furthermore, comparison of values of maximum packing fractions obtained from our experiments with simulations performed by Phillipse *et al.* showed that the maximum packing fraction values were closer to those for randomly packed, rather than highly ordered, microstructures. Numerical simulations will help answer questions regarding the microstructure in these flows.

It has been established that the microstructure of concentrated suspensions is affected by, and has an effect on, the imposed flows. There is limited work that investigates this non-linear relationship for a variety of flows. To quantify the dynamics of the microstructure in concentrated fiber suspensions, experiments were performed using an oscillatory pipe flow. Shear-induced migration is a noticeable manifestation of the irreversible dynamics in the microstructure of concentrated suspensions. Although this phenomena has been studied for spheres [73], similar studies for non-spherical particles is lacking. The only evidence of particle migration was shown via experiments performed by Mondy [10] in Couette flows. Chapter 3 highlights quantifiable evidence of shear-induced migration of non-spherical particles in pipe flows.

Experiments described in Section 3.1 form the first set of experiments to show non-spherical particle migration in more general flows. These experiments are also the first measurements of the orientation distribution of fibers in pressure-driven flows, using direct optical imaging techniques (described in Section 3.2). Results shown in Section

3.3 show migration for suspensions at particle volume fractions as low as 5.5 %, which is significantly lower than the threshold for spheres. We also observe that the fibers have a distinct preferential alignment in the flow direction (see Subsection 3.3.3), though we expect to observe an inhomogenous orientation distribution, wherein the fibers near the walls will be preferentially aligned in the vorticity direction, while the fibers near the center will be aligned with the flow. This vorticity alignment is not a surprising result and has been shown to occur via direct numerical simulations in shearing flows [11].

Similar to the rheology, future work about the dynamics will predict the microstructure of concentrated suspensions of rigid rods in pressure-driven flows. These simulations will be used to confirm the occurrence of shear-induced migration as well as predict the ranges of parameters, like strain amplitude and bulk initial concentration over which this phenomena occurs. It has been shown that collective motion like particle migration affects the orientation distribution, and numerical simulations will be used to quantify this effect. The suspension balance model has been shown to work well to predict shear induced migration in suspensions of spheres, and will hence be used in an attempt to model this phenomena in suspensions of rigid rods. Further questions regarding the effect of confinement on particle migration, as well as its effect on the orientation distribution, can also be answered via this approach.

A framework for experiments and data analyses has been provided to study these systems, and our results look promising. This work will take us one step closer to generating an accurate continuum model for these systems.

# APPENDIX A
# RIGIDITY TESTS FOR NON-SPHERICAL PARTICLES

We make a simplifying assumption that the fibers used in the experiments are rigid: they do not bend nor stretch under the forces and stresses imposed by the flow. In this appendix, criteria that have been developed for estimating the flow fields at which this assumption may fail.

Forgacs and Mason [87] developed a theory for the critical stress, $\Sigma_{crit}$, at which a rod will buckle in an axial compression flow. For a fiber of aspect ratio, $A = L/d$, where $L$ and $d$ are the length and diameter, the stress was estimated as,

$$\Sigma_{crit} \cong \frac{E_b[ln(2A) - 1.75]}{2A^4}, \tag{A-1}$$

where $E_b$ is the bending modulus, a value that is approximately twice the Young's modulus of the fiber. To confirm the theory, Forgacs and Mason [87] measured the bending of polymer fibers, having a range of bending moduli, as a function flow strength. They reported good agreement between the qualitative observations and the predicted value of $\Sigma_{crit}$. Generally, any deformation of a fiber is argued to be negligible when the maximum stress that a hydrodynamic flow exerts is much smaller than the critical stress given by A-1. For a shearing flow, the maximum stress ($\Sigma_{max}$) can be approximated by the product of the fluid viscosity, $\eta_f$ and maximum value of the rate of shear, $\dot{\gamma}$.

Switzer and Klingenberg [88] simulated a micromechanical model of flexible fibers and calculated the dynamics and rheology. They definded a restoring torque, $\boldsymbol{Y}_i$, that included the elastic forces due to bending as well as twisting of the fiber. For each segment $i$ of a discretized fiber, the restoring torque was defined as

$$|\boldsymbol{Y}_i| = \kappa_b(\theta_i - \theta_i^{eq}) + \kappa_t(\phi_i - \phi_i^{eq}), \tag{A-2}$$

where the bending angle, $\theta_i$, and twisting angle, $\phi_i$, of the segment are referenced to their equilibrium values, $\theta_i^{eq}$ and $\phi_i^{eq}$ respectively. The constant $\kappa_b = E_y I/l_i$ is the bending

constant of the fiber, which depends upon the Young's modulus for the fiber ($E_y$), the area moment of the fiber ($I = \pi r^4/4$ with $r$ the diameter), and the length of the segment $i$ ($l_i$). Likewise, the twisting constant, $\kappa_t$ is calculated from the Poisson ratio. Simulations were performed for a range of values of the effective stiffness, $S^{eff}$,

$$S^{eff} = \frac{E_y I}{4\eta_f \dot{\gamma} L^4}, \tag{A-3}$$

a dimensionless parameter that compares the bending and hydrodynamic forces. Utilizing the definition of $I$ and the aspect ratio, the equation can be rewritten as

$$S^{eff} = \frac{E_y \pi}{64\eta_f \dot{\gamma} A^4}, \tag{A-4}$$

which has a similar dependence on the fiber properties and fluid stress as $\Sigma_{crit}/\Sigma_{max}$ as defined by Forgacs and Mason [87], save for the logarithmic correction. As $S^{eff} \to \infty$, the fibers are considered rigid.

Lauga *et al.* [89] and others [90] characterized the buckling instability using the sperm number, $S_p$, as

$$S_p = \frac{8\eta_f \dot{\gamma} A^4}{E_y}, \tag{A-5}$$

which arises from the ratio of the viscous forces ($\sim \eta_f \dot{\gamma} L^2/2$) to the elastic forces ($\sim E_y r^4/L^2$) [91]. The sperm number definition has an inverse dependence on the fiber properties and the fluid flow to the value of $S^{eff}$. For the specific case of a cellular flow, Wandersman *et al.* [90] quantified the point at which a fiber would buckle, and found that the probability goes to zero as $S_p$ drops below 120. Young and Shelley [92] developed a correction to the elasto-viscous number (i.e. sperm number) utilizing slender body theory. As a result, they produced a dimensionless parameter,

$$S_p^* = \frac{128\eta \dot{\gamma} A^4}{E_y[ln(2A) - 0.5]}, \tag{A-6}$$

that included a logarithmic dependence on the aspect ratio, similarly to the original work of Forgacs and Mason [87]. For a fiber in a cellular flow, the criteria for rigidity was found to be $S_p^* \sim 400$, with lower values being rigid [92].

# APPENDIX B
# CALCULATIONS AND CALIBRATIONS OF PRESSURE-IMPOSED RHEOLOGY DATA

The goal of the rheology experiments is the determination of the relationship between properties such as shear stress ($\tau$), particle pressure ($P^p$), and volume fraction ($\phi$) for dense suspensions of rigid fibers. These quantities are calculated using values of torque ($T$), normal force ($F_n$), and gap height ($h$) measured from the shear cell shown in Figure B-1. In this device, the fluid is filled to a height $h_f$ in a cylindrical annulus of inner and outer radii $R_1 = 44$ mm and $R_2 = 90$ mm; the maximum fill height $h_f = 22$ mm. A porous plate that allows fluid to pass through, but not particles, is submerged into the fluid to an adjustable height $h$. To generate a shearing flow, the cylindrical annulus is affixed to a plate that can rotate at angular velocities $\omega$ between 0.1 to 0.7 rad/s while the porous plate remains fixed. Hence, the direction of flow is angular and the gradient direction is parallel with gravity. Both the torque $T$ and normal force $F_n$ are measured by transducers attached to the top plate. Limits of the transducers for the measurement of torque are 0.01 to 1.2 N·m, and the lowest accurate measurement of normal force is 0.8 N.

The major advantage of performing rheological measurements in the custom-built rheometer shown in Figure B-1 is that experiments can be performed in two different modes: volume-controlled and pressure-controlled rheology. In volume-controlled experiments, the height $h$ of the porous plate is fixed at a specified value, while in pressure-imposed rheology experiments, $h$ is adjusted through a feedback control mechanism during the experiment in order to maintain the normal force $F_n$ at a set value.

Due to the nature of the experimental setup and physical constraints, various corrections are made to the raw data obtained from the experimental device to derive the desired parameters. These treatments are described below.

## B.1 Height, Volume Fraction, and Number Density

The simplest relationship is between the height of the top-plate and the resultant particle volume fraction. A suspension, of known volume fraction $\phi_i$, is added to the rheometer to a fill height of $h_f$. Note that all heights are measured from the bottom of the cell. The particle volume fraction, $\phi$, is now determined from the set height $h$ as

$$\phi = \frac{\phi_i h_f}{h}. \tag{B-1}$$

In certain cases, the volume fraction of rod-like particles is expressed in terms of a dimensionless number density $nL^2d$, where the number density $n = N/V$ is calculated using the number of particles $N$ per unit volume $V$, where the particles have a length $L$ and diameter $d$. The relation between this dimensionless number density and the volume fraction is

$$\phi = \left(nL^2d\right)\left(\frac{\pi}{4A}\right), \tag{B-2}$$

where the aspect ratio $A = L/d$.

## B.2 Torque and Stress Calculations

The value of the torque $T$ measured by the rheometer is higher than the value of the torque exerted by the suspension $T_b$. Corrections are made to the measured values of torque to account for the mechanical losses experienced by the system, $T_0$, and the torque exerted by the fluid in the narrow gap between the movable top plate of the rheometer and the walls of the annular cell, $T_g$, as shown in Figure B-1. To evaluate these corrections, the rheometer is calibrated using the suspending fluid in the absence of particles. The equation for the corrections to the measured torque can be written as

$$T = T_0 + T_g + T_b. \tag{B-3}$$

The mechanical losses are assumed to have a component that is constant and a component that is proportional to the rotation rate $\omega$. Since the suspending fluid is Newtonian, the torque contributions $T_g$ and $T_b$ are proportional to $\omega$. As the height is

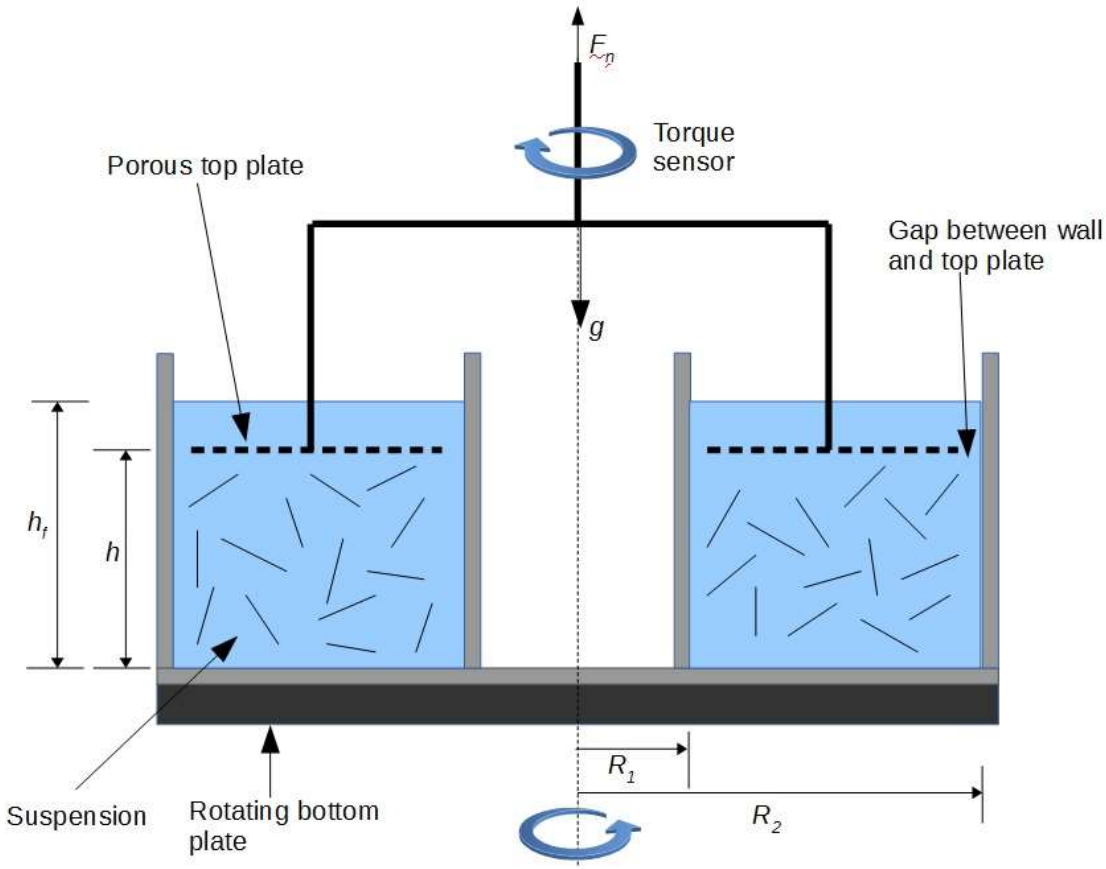


Figure B-1. Schematic of the rheometer cell. The top plate is porous, can be moved only in the vertical direction, and is always kept submerged during the experiment. The bottom portion of the rheometer cell is fixed to a base that can be rotated at a controlled value $\omega$, while the torque $T$ and normal force $F_n$ are measured on the shaft attached to the top plate. The schematic also shows the gap between the edge of the top plate and the inner wall of the annular cell (not drawn to scale), which allows for the unhindered movement of the plate. The gap is sufficiently small that particles can not pass through it.

changed, neither $T_0$ nor $T_g$ are affected. However, the shear rate, and hence torque, is inversely proportional to the height in the bulk region of the rheometer. Including these relations in Equation B-3 gives

$$T = a + b\omega + \frac{c\omega}{h}, \tag{B-4}$$

where $a$, $b$, and $c$ are constants. The values of $a$ and $b$ are determined by performing a least-squares fit to measurements of $T$ for a span of values of $\omega$ and $h$. Of course $c$ is also determined from the analysis, but this value is not needed for the further developments. Furthermore, the values of $a$ and $b$ are assumed to not change so long as the suspending fluid is not altered.

Particles are added to the suspending fluid once the corrections are determined from the experiments on the fluid in the absence of the particles. Then the torque due to the suspension at any value of $\omega$ and $h$ is calculated from the measured torque $T(\omega, h)$ by using the corrections,

$$T_b(\omega, h) = -(a + b\omega) + T(\omega, h). \tag{B-5}$$

The goal is to relate the torque $T_b(\omega, h)$ to the suspension stress, which is a function of the rate of shear and volume fraction, $\tau(\dot{\gamma}, \phi)$. The net torque exerted by the bulk of the suspending fluid is given by integrating the product of the shear stress and radial distance from the rotation axis over the top plate,

$$T_b(\omega, h) = \int_S \tau(\dot{\gamma}, \phi)\, r dS. \tag{B-6}$$

It is convenient to work in the cylindrical coordinate system where, after integrating over the angular coordinate,

$$T_b(\omega, h) = 2\pi \int_{r=R_1}^{R_2} \tau(\dot{\gamma}, \phi)\, r^2 dr. \tag{B-7}$$

In all that follows, it is assumed that the rate of shear at any radial position can be related simply to the rotation rate and the height of the plate through

$$\dot{\gamma}(r) = \frac{\omega r}{h}. \tag{B-8}$$

This assumption ignores the influence of the side walls at $r = R_1$ and $R_2$ on the flow profile. Also, all measurements are recorded only after the flow profile and associated torque have attained a steady state value, hence the time-dependent properties of the shear rate are not required.

Equation B-7 is ill-posed, as are all integral equations, since the unknown appears within the integrand. Solving requires regularizing the problem by imposing a functional form on the unknown stress. One approach is to assume that the suspension follows a generalization of the Newtonian fluid constitutive law. In previous work using this device on concentrated suspensions of spheres, that approach was utilized [63]. However, published experimental results have consistently demonstrated that suspensions of rigid rods shear-thin [93]. Consequently, here we consider both a generalized Newtonian fluid model and a more general one.

### B.2.1 Generalized Newtonian fluid model

In the generalized Newtonian model, the stress of the suspension is assumed to scale linearly with the rate of shear. As a convenient reference point, all results obtained from the experiments are reported based upon values of shear rate at the midpoint of the annulus,

$$\dot{\gamma}_c = \frac{\omega (R_1 + R_2)}{2h}, \tag{B-9}$$

where the stress is $\tau(\dot{\gamma}_c)$. Consequently, the stress at any radial position in the cell can be written as

$$\tau(r) = \frac{2\tau(\dot{\gamma}_c)\, r}{(R_1 + R_2)}. \tag{B-10}$$

After substituting this into Equation B-7, integrating, and then solving, the stress can be related to the torque measured at the rotation rate $\omega$,

$$\tau\left(\dot{\gamma}_c\right) = \frac{T_b\left(R_1 + R_2\right)}{\pi(R_2^4 - R_1^4)}. \tag{B-11}$$

Using Equation B-11 we can now calculate the shear stress generated by the suspension for different shear rates measured via different rotation rates $\omega$ and heights $h$.

### B.2.2 General Stress Model

An alternative approach to calculating the stress assumes a more general form of the constitutive law used to regularize the integral equation (Equation B-7). In this method, the stress is linearized around the value of the stress at the center of the cell where the rate of shear is $\dot{\gamma}_c = \omega(R_1 + R_2)/2h$,

$$\tau\left(\dot{\gamma}\right) = \tau\left(\dot{\gamma}_c\right) + \left(\dot{\gamma} - \dot{\gamma}_c\right) \left.\frac{\partial \tau}{\partial \dot{\gamma}}\right|_{\dot{\gamma}_c}. \tag{B-12}$$

Substituting into Equation B-7 and integrating gives

$$T\left(\omega\right) = 2\pi \left[A\tau\left(\dot{\gamma}_c\right) + \left(B\right|_{\omega} - \dot{\gamma}_c A\right) \left.\frac{\partial \tau}{\partial \dot{\gamma}}\right|_{\dot{\gamma}_c}\right], \tag{B-13}$$

where

$$A = \int_{r=R_1}^{R_2} r^2 dr \tag{B-14}$$

and

$$B\left|_{\omega}\right. = \int_{r=R_1}^{R_2} \frac{\omega r^3}{h} dr. \tag{B-15}$$

To eliminate the gradient of the stress with respect to the rate of shear, a second measurement of the torque is made at a rate of rotation that is different by a differential amount $\delta\omega$,

$$T\left(\omega + \delta\omega\right) = 2\pi \left[A\tau\left(\dot{\gamma}_c\right) + \left(B\right|_{\omega+\delta\omega} - \dot{\gamma}_c A\right) \left.\frac{\partial \tau}{\partial \dot{\gamma}}\right|_{\dot{\gamma}_c}\right]. \tag{B-16}$$

Solving for $\partial\tau/\partial\dot{\gamma}|_{\dot{\gamma}_c}$, then dividing by the differential rotation rate $\delta\omega$ and taking the limit as it goes to zero gives

$$\left.\frac{\partial\tau}{\partial\dot{\gamma}}\right|_{\dot{\gamma}_c} = \frac{1}{2\pi}\left(\left.\frac{\partial B\left(\omega\right)}{\partial\omega}\right|_{\omega}\right)^{-1}\left.\frac{\partial T\left(\omega\right)}{\partial\omega}\right|_{\omega}. \tag{B-17}$$

Using this result, an explicit expression for the stress can be calculated as

$$\tau\left(\dot{\gamma}_c\right) = \frac{1}{2\pi A}\left[T\left(\omega\right) + \left(\dot{\gamma}_c A - B|_{\omega}\right)\left(\left.\frac{\partial B\left(\omega\right)}{\partial\omega}\right|_{\omega}\right)^{-1}\left.\frac{\partial T\left(\omega\right)}{\partial\omega}\right|_{\omega}\right]. \tag{B-18}$$

Evaluating the integrals $A$ and $B$, as well as the gradient of $B$, gives the explicit expression for the stress,

$$\tau\left(\dot{\gamma}_c\right) = \frac{3}{2\pi\left(R_2^3 - R_1^3\right)}\left[T\left(\omega\right) + \left(\frac{2\left(R_1 + R_2\right)\left(R_2^3 - R_1^3\right) - 3\left(R_2^4 - R_1^4\right)}{3\left(R_2^4 - R_1^4\right)}\right)\omega\left.\frac{\partial T\left(\omega\right)}{\partial\omega}\right|_{\omega}\right]. \tag{B-19}$$

For a suspension system that follows a generalized Newtonian law, the result given by evaluating Equation B-19 reduces to the result derived by assuming a Newtonian fluid from the outset (Equation B-11).

### B.3 Normal Force Measurements

When concentrated suspensions of rigid, non-colloidal particles, are acted upon by an imposed flow, they exhibit non-Newtonian behavior at high particle volume fractions. The existence of normal stresses is one example of non-Newtonian phenomena. Two mechanisms possibly contribute to normal stresses in suspensions: hydrodynamic contributions and contributions due to contacts between particles. For suspensions of rods, calculations have indicated that the normal stresses are weak and are overwhelmingly due to contacts [11]. However, hydrodynamics are an essential part of the problem still, since the contact interactions depend on the microstructure of the suspension and the flow is responsible for altering the microstructure.

In our rheology experiments, a concentrated suspension is sheared resulting in the hindered rotation of rods due to contacts between near neighbors. The contact forces that this motion causes results in a force chain between the particles. A dense network

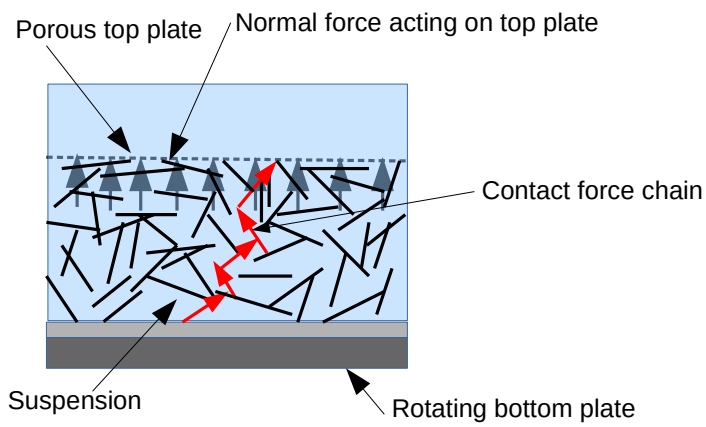


Figure B-2. Schematic showing forces exerted by the rods on the top plate. A small mesh size allows the fluid to move freely across the top-plate and maintains a constant mass of particles in the cell. Contact force chains are caused by high number**s** of contacts between particles at high particle volume fractions.

of these force chains occur in a dense suspension at high volume fractions due to the large number of particle contacts. These force networks exert a normal force on the top plate of the rheometer, as visualized in Figure B-2.

The rheometer can measure this normal force using a force transducer contained in an accurate balance. The normal force exerted by the fluid is not equivalent to the force measured by the instrument. In addition to the corrections to the torque described previously, calibration experiments using only the suspending fluid are used to obtain corrections to the normal force as well. It is assumed that since the fluid is Newtonian, it does not exert any normal force on the top plate. The value obtained from the force transducer $F$ measured by the balance includes the force exerted by weight of the top-plate $F_t$ and the buoyancy force $F_b$ exerted by the fluid on the plate. The weight of the plate is constant and can be removed directly from the measured force. The correction for the buoyancy force depends depends on the height $h$: the top plate must

be completely submerged in the fluid for the entire duration of the experiment, but as the height changes, more (or less) of the brackets that support the weight of the plate $F_t$ are submerged. Consequently, the buoyancy correction is simply determined from the calibration experiment and used to correct the measure force,

$$\hat{F}_n = F - F_t + F_b, \tag{B-20}$$

where $\hat{F}_n$ is the normal force exerted on the top plate of the rheometer. An expression for the resulting pressure $P^p$ on the plate is given by

$$P^p = \frac{\hat{F}_n}{\pi(R_2^2 - R_1^2)}. \tag{B-21}$$

# APPENDIX C
# UNIFYING RHEOLOGY OF DENSE SUSPENSIONS AND GRANULAR MEDIA

Universal constitutive laws have been proposed for dense granular flows [94, 95, 96]. Boyer *et al.* demonstrated that dense suspensions of hard spheres of diameter $d$ and density $\rho_p$ sheared at a rate of $\dot{\gamma}$ under a confining pressure $P^p$ can be treated using similar constitutive equations as granular media. Applying granular concepts to dense suspensions requires modifications to the experimental methods.

In the case of dense granular media of spherical particles, one dimensionless number, can be used as a control variable: $I = d\sqrt{\rho_p/P^p}\dot{\gamma}$. This inertial number $I$ is a ratio between the inertial time of rearrangement, $t_{micro} = d\sqrt{\rho_p/P^p}$, and the time scale of the strain $t_{macro} = 1/\dot{\gamma}$. The granular rheology is then described using two functions of the inertial number for a wide range of flows: the shear stress $\tau = \mu(I)P^p$, and volume fraction, $\phi = \phi(I)$.

Boyer *et al.* demonstrated that these ideas could be applied to dense suspensions of hard spheres [63] with a few modifications. From a physical standpoint, the experiments must be modified by allowing the suspending fluid to pass through the boundary of the shearing cell. This enables compression of the particle phase. In this case of viscous suspensions of hard spheres, the theory must be modified by considering the dominant forces that are viscous rather than inertial since the Stokes number $St = \rho_p d^2\dot{\gamma}/\eta_f$ is small. The internal time of rearrangement can be defined using a viscous scaling as $t_{micro} = \eta_f/P^p$. This system can now be characterized using a dimensionless viscous number $J$ as

$$J = \frac{\eta_f \dot{\gamma}}{P^p}, \tag{C-1}$$

where $\eta_f$ is the viscosity of the suspending fluid. Macroscopic properties like the coefficient of friction, $\mu$, and the volume fraction, $\phi$, should now be functions of $J$ alone,

$$\tau = \mu(J)P^p \quad \text{and} \quad \phi = \phi(J). \tag{C-2}$$

Conventional rheology experiments are performed using a controlled volume. However, these volume-controlled experiments can be reconciled with the above-described pressure-controlled experiments. When a suspension is sheared at a constant volume fraction, shear and normal stresses scale viscously as $\eta_f \dot{\gamma}$ and can be expressed as functions of $\phi$

$$\tau = \eta_s(\phi)\eta_f\dot{\gamma} \quad \text{and} \quad P^p = \eta_n(\phi)\eta_f\dot{\gamma}, \tag{C-3}$$

where $\eta_s(\phi)$ and $\eta_n(\phi)$ are the dimensionless shear and normal viscosities, respectively [97, 82]. Relations can be drawn in terms of the dimensionless viscous number $J$ to determine the particle pressure and the shear stress as

$$P^p = \frac{1}{J(\phi)}\eta_f\dot{\gamma} \quad \text{and} \quad \tau = \frac{\mu[J(\phi)]}{J(\phi)}\eta_f\dot{\gamma}. \tag{C-4}$$

Furthermore, this can be used with Equation C-3 which gives

$$\eta_s(\phi) = \frac{\mu[J(\phi)]}{J(\phi)} \quad \text{and} \quad \eta_n(\phi) = \frac{1}{J(\phi)}. \tag{C-5}$$

REFERENCES


[1] R.G. Larson. *The Structure and Rheology of Complex Fluids*. OUP USA, 1999.

[2] M. Hassanpoura, P. Shafighb, and H.B. Mahmudb. Lightweight aggregate concrete fiber reinforcement – A review. *Constr. Build. Mater.*, 37:452–461, 2012.

[3] C.H. Bivens, C. Boney, C. Fredd, J. Lassek, P. Sullivan, J. Engels, E.O. Fielder, T. Gorham, T. Judd, A.E.S. Mogollon, L. Tabor, A.V. Munoz, and D. Willberg. New fibers for hydraulic fracturing. *Oilfield Review (published by Schlumberger Ltd.)*, Summer Issue:34–43, 2005.

[4] R. Elgaddafi, R. Ahmed, M. George, and F. Growcock. Settling behavior of spherical particles in fiber-containing drilling fluids. *J. Petr. Sci. Engr.*, **84–85**:20–28, 2012.

[5] A Acrivos. Bingham Award Lecture–1994 Shear-induced particle diffusion in concentrated suspensions of noncolloidal particles. *J. Rheol.*, 39:813–826, 1995.

[6] D. Leighton and A. Acrivos. The shear-induced migration of particles in concentrated suspensions. *J. Fluid Mech.*, 181:415–439, 1987.

[7] D. Leighton and A. Acrivos. Measurement of shear-induced self-diffusion in concentrated suspensions of spheres. *J. Fluid Mech.*, **177**:109–131, 1987.

[8] R. J. Phillips, R. C. Armstrong, R. A. Brown, A. L. Graham, and J. R Abbott. A constitutive equation for concentrated suspensions that accounts for shear-induced particle migration. *Phys. Fluids A: Fluid Dynamics*, **4**(1):30–40, 1992.

[9] P. R. Nott and J. F. Brady. Pressure-driven flow of suspensions: simulation and theory. *J. Fluid Mech.*, **275**:157–199, 1994.

[10] L. A. Mondy, H Brenner, S. A. Altobelli, J. R. Abbott, and A. L. Graham. Shear-induced particle migration in suspensions of rods. *J. Rheol.*, **38**(2):444–452, 1994.

[11] B. Snook, L. M. Davidson, J. E. Butler, O. Pouliquen, and E. Guazzelli. Normal stress differences in suspensions of rigid fibres. *J. Fluid Mech.*, **758**:486–507, 2014.

[12] M. Keshtkar, M.C. Heuzey, and P.J. Carreau. Rheological behavior of fiber-filled model suspensions: Effect of fiber flexibility. *J. Rheol.*, **53**:631–650, 2009.

[13] S. Bounoua, P. Kuzhir, and É. Lemaire. Normal stress differences in non-Brownian fiber suspensions. *J. Rheol.*, **60**(4):661–671, 2016.

[14] J. Park, J. M. Bricker, and J. E. Butler. Cross-stream migration in dilute solutions of rigid polymers undergoing rectilinear flow near a wall. *Phys.Rev. E*, **76**:040801(R), 2007.

[15] J. Park and J. E. Butler. Inhomogeneous distribution of a rigid fibre undergoing rectilinear flow between parallel walls at high Peclet numbers. *J. Fluid Mech.*, **630**:267298, 2009.

[16] R. Hsu and P. Ganatos. Gravitational and zero-drag motion of a spheroid adjacent to an inclined plane at low Reynolds number. *J. Fluid Mech.*, **268**:267, 1976.

[17] G. B. Jeffery. The motion of ellipsoidal particles immersed in a viscous fluid. *Proc. R. Soc. London A*, **102**:161–179, 1922.

[18] F. P. Bretherton. The motion of rigid particles in a shear flow at low Reynolds number. *J. Fluid Mech.*, **14**:284, 1962.

[19] B. J. Trevelyan and S. G. Mason. Particle motions in sheared suspensions. I. Rotations. *J. Colloid Sci.*, **6**:354, 1951.

[20] S. G. and R. J. Manley. Particle motions in sheared suspensions: Orientations and interactions of rigid rods. *Proc. R. Soc. London, Ser. A*, **238**:117, 1956.

[21] G. K. Batchelor. Slender-body theory for particles of arbitrary cross-section in Stokes flow. *J. Fluid Mech.*, **44**:419–440, 1970.

[22] R. G. Cox. The motion of long slender bodies in a viscous fluid. Part 1. General theory. *J. Fluid Mech.*, **44**:791–810, 1970.

[23] M. Doi and S. F. Edwards. *The Theory of Polymer Dynamics*. Oxford University Press: New York, 1986.

[24] J. E. Butler. Collective dynamics of particles in viscous flows with an emphasis on slender rods. In *Collective Dynamics of Particles*, pages 99–128. Springer, 2017.

[25] S. Kim and S. J. Karrila. *Microhydrodynamics: Principles and Selected Applications*. Butterworth-Heineman, 2005.

[26] G. K. Batchelor. The stress generated in a non-dilute suspension of elongated particles by pure straining motion. *J. Fluid Mech.*, **46**:813–829, 1971.

[27] M. B. Mackaplow and E. S. G. Shaqfeh. A numerical study of the rheological properties of suspensions of rigid, non-Brownian fibres. *J. Fluid Mech.*, 329:155–186, 1996.

[28] A. Salahuddin and C. K. Wu, J.and Aidun. Study of semidilute fibre suspension rheology with lattice-Boltzmann method. *Rheologica Acta*, **52**(10-12):891–902, 2013.

[29] X. Fan, N. Phan-Thien, and R. Zheng. A direct simulation of fibre suspensions. *J. Non-Newtonian Fluid Mech.*, **74**:113–135, 1998.

[30] Braden Snook. *The dynamics of the microstructure and the rheology in suspensions of rigid particles*. PhD thesis, University of Florida, Gainesville, FL, 2015.

[31] Y. Yamane, Y. Kaneda, and M. Dio. Numerical simulation of semi-dilute suspensions of rodlike particles in shear flow. *J. Non-Newtonian Fluid Mech.*, **54**:405–421, 1994.

[32] C. A. Stover, D. L. Koch, and C. Cohen. Observations of fibre orientation in simple shear flow of semi-dilue suspensions. *J. Fluid Mech.*, **238**:277–296, 1992.

[33] R. L. Powell. Rheology of suspensions of rodlike particles. *J. Stat. Phys.*, **62**, 1991.

[34] E. Ganani and R. L. Powell. Suspensions of rodlike particles: Literature review and data correlations. *J. Comp. Mat.*, **19**:194–215, 1984.

[35] S. M. Dinh and R. C. Armstrong. A rheological equation of state for semiconcentrated fiber suspensions. *J. Rheol.*, **28**:207–227, 1984.

[36] E. S. G. Shaqfeh and H. Fredrickson. The hydrodynamic stress in a suspension of rods. *Phys. Fluids A*, **2**:7–24, 1990.

[37] R. L. Schiek and E. S. G. Shaqfeh. A nonlocal theory for stress in bound, Brownian suspensions of slender, rigid fibers. *J. Fluid Mech.*, **296**:271–324, 1995.

[38] M. A. Bibbo, S. M. Dinh, and R. C. Armstrong. Shear flow properties of semiconcentrated fiber suspensions. *J. Rheol.*, **29**:905–929, 1985.

[39] R. O. Maschmeyer and C. T. Hill. Rheology of concentrated suspensions of fibers in tube flow. II. An exploratory study. *Trans. Soc. Rheol.*, **21**:183–195, 1977.

[40] M. Sepehr, P. J. Carreau, M. Moan, and G. Ausias. Rheological properties of short fiber model suspensions. *J. Rheol.*, **48**:1023–1048, 2004.

[41] C. P. J. Bennington, R. J. Kerekes, and J. R. Grace. The yield stress of fibre suspensions. *Can. J. Chem. Eng.*, **68**:748–757, 1990.

[42] D. Leighton and A. Acrivos. The shear-induced migration of particles in concentrated suspensions. *J. Fluid Mech.*, **181**:415–439, 1987.

[43] A. Karnis, H. Goldsmith, and S. Mason. The kinetics of flowing dispersions: I. Concentrated suspensions of rigid particles. *J. Colloid Interface Sci.*, **22**:531–553, 1966.

[44] J. E. Butler, P. D. Majors, and R. T. Bonnecaze. Shear-induced particle migration for oscillatory flow of a suspension within a tube. *Phys. Fluids*, **11**:2865–2877, 1999.

[45] R. E. Hampton, A. A. Mammoli, A. L. Graham, N. Tetlow, and S. A. Altobelli. Migration of particles undergoing pressure-driven flow in a circular conduit. *J. Rheol.*, **41**(3):621–640, 1997.

[46] S. A. Altobelli, R. C. Givler, and E. Fukushima. Velocity and concentration measurements of suspensions by nuclear magnetic resonance imaging. *J. Rheol.*, **35**:721–734, 1991.

[47] C. J. Koh, P. Hookham, and L. G. Leal. An experimental investigation of concentrated suspension flows in a rectangular channel. *J. Fluid Mech.*, **266**:132, 1994.

[48] M. K. Lyon and L. G. Leal. An experimental study of the motion of concentrated suspensions in two-dimensional channel flow. Part 1: Monodisperse systems. *J. Fluid Mech.*, **363**:2556, 1998.

[49] J. T. Norman, H. V. Nayak, and R. T. Bonnecaze. Migration of buoyant particles in low-Reynolds-number pressure-driven flows. *J. Fluid Mech.*, **523**:135, 2005.

[50] A. Okagawa, R. G. Cox, and S. G. Mason. The kinetics of flowing dispersions. VI. Transient orientation and rheological phenomena of rods and discs in shear flow. *J. Colloid Interface Sci.*, **45**(2):303–329, 1973.

[51] D. J. Pine, J. P. Gollub, J. F. Brady, and A. M. Leshansky. Chaos and threshold for irreversibility in sheared suspensions. *Nature*, **438**:997, 2005.

[52] F. R. Da Cunha and E. J. Hinch. Shear-induced dispersion in a dilute suspension of rough spheres. *J. Fluid Mech.*, **309**:211223, 1996.

[53] G. Drazer, J. Koplik, B. Khusid, and A. Acrivos. Deterministic and stochastic behaviour of non-brownian spheres in sheared suspensions. *Journal of Fluid Mechanics*, **460**:307–335, 2002.

[54] B. Metzger, P. Pham, and J. E. Butler. Irreversibility and chaos: Role of lubrication interactions in sheared suspensions. *Phys. Rev. E*, **87**:052304, May 2013.

[55] E. Ganani and R. L. Powell. Suspensions of rodlike particles: Literature review and data correlations. *J. Composite Mater.*, **19**:194–215, 1985.

[56] A. Mongruel and M. Cloitre. Shear viscosity of suspensions of aligned non-Brownian fibres. *Rheologica Acta*, **38**(5):451–457, November 1999.

[57] M. Chaouche and D. L. Koch. Rheology of non-Brownian rigid fiber suspensions with adhesive contacts. *J. Rheol.*, **45**(2):369–382, March 2001.

[58] S. Bounoua, E. Lemaire, J. Férec, G. Ausias, A. Zubarev, and P. Kuzhir. Apparent yield stress in rigid fibre suspensions: The role of attractive colloidal interactions. *J. Fluid Mech.*, **802**:611–633, August 2016.

[59] S. Bounoua, É. Lemaire, J. Férec, G. Ausias, and P. Kuzhir. Shear-thinning in concentrated rigid fiber suspensions: Aggregation induced by adhesive interactions. *J. Rheol*, **60**(6):1279–1300, 2016.

[60] M. A. Bibbó. *Rheology of semiconcentrated fiber suspensions*. PhD thesis, Massachusetts Institute of Technology, 1987.

[61] R. Sundararajakumar and D. L. Koch. Structure and properties of sheared fiber suspensions with mechanical contacts. *J. Non-Newtonian Fluid Mech.*, **73**:205–239, 1997.

[62] M. P. Petrich and D. L. Koch. Interactions between contacting fibers. *Phys. Fluids*, **10**(8):2111–2113, 1998.

[63] F. Boyer, É. Guazzelli, and O. Pouliquen. Unifying suspension and granular rheology. *Phys. Rev. Lett.*, **107**(18):188301, October 2011.

[64] S. Dagois-Bohy, S. Hormozi, É. Guazzelli, and O. Pouliquen. Rheology of dense suspensions of non-colloidal spheres in yield-stress fluids. *J. Fluid Mech.*, **776**:R2, July 2015.

[65] L. E. Becker and M. J. Shelley. Instability of elastic filaments in shear flow yields first normal stress differences. *Phys. Rev. Lett.*, **87**(19):198301, 2001.

[66] Y. N. Young and M. J. Shelley. Stretch-coil transition and transport of fibers in cellular flows. *Phys. Rev. Lett.*, **99**(5):58303, 2007.

[67] O. Rahli, L. Tadrist, and R. Blanc. Experimental analysis of the porosity of randomly packed rigid fibers. *C. R. Acad. Sci., Ser. IIb: Mec., Phys., Chim., Astron.*, **327**(8):725–729, October 1999.

[68] S. R. Williams and A. P. Philipse. Random packings of spheres and spherocylinders simulated by mechanical contraction. *Phys. Rev. E*, **67**(5):051301–9, May 2003.

[69] J. R. Abbott, N. Tetlow, A. L. Graham, S. A. Altobelli, Eiichi Fukushima, L. A. Mondy, and T. S. Stephens. Experimental observations of particle migration in concentrated suspensions: Couette flow. *J. Rheol.*, **35**(5):773–795, 1991.

[70] A. W. Chow, S. W. Sinton, J. H. Iwamiya, and T. S. Stephens. Shearinduced particle migration in couette and parallelplate viscometers: Nmr imaging and stress measurements. *Phys. Fluids*, **6**(8):2561–2576, 1994.

[71] N. Tetlow, A. L. Graham, M. S. Ingber, S. R. Subia, L. A. Mondy, and S. A. Altobelli. Particle migration in a couette apparatus: Experiment and modeling. *J. .Rheol.*, **42**(2):307–327, 1998.

[72] Z. Fang and N. Phan-Thien. Numerical simulation of particle migration in concentrated suspensions by a finite volume method. *Journal of Non-Newtonian Fluid Mechanics*, **58**(1):67 – 81, 1995.

[73] B. Snook, J. E. Butler, and É. Guazzelli. Dynamics of shear-induced migration of spherical particles in oscillatory pipe flow. *J. Fluid Mech.*, **786**:128–153, 2016.

[74] M. S. Ingber, Vorobieff P. Mammoli, A. A., T. McCollam, and A. L. Graham. Experimental and numerical analysis of irreversibilities among particles suspended in a couette device. *J. Rheol.*, **50**(2):99–114, 2006.

[75] P. Pham, B. Metzger, and J. E. Butler. Particle dispersion in sheared suspensions: Crucial role of solid-solid contacts. *Phys. Fluids*, **27**:051701, 2015.

[76] I. M. Janosi, T. Tel, D. E. Wolf, and J. A. C. Gallas. Chaotic particle dynamics in viscous flows: The three-particle Stokeslet problem. *Phys. Rev. E*, **65**:2858–2868, 1997.

[77] B. Metzger and J. E. Butler. Irreversibility and chaos: Role of long range hydrodynamic interactions in sheared suspensions. *Phys. Rev. E*, **82**:051406, 2010.

[78] B. Metzger, P. Pham, and J. E. Butler. Irreversibility and chaos: Role of lubrication interactions in sheared suspensions. *Phys. Rev. E*, **87**, 2013.

[79] K. Yeo and M. R. Maxey. Numerical simulations of concentrated suspensions of mono-disperse particles in a Poiseuille flow. *J. Fluid Mech.*, **682**:491–518, 2011.

[80] I. M. Krieger. Rheology of monodisperse latices. *Adv. Coll. Interface Sci.*, **3**(2):111–136, 1972.

[81] J. M. Bricker and J. E. Butler. Oscillatory shear of suspensions of noncolloidal particles. *J. Rheol.*, **50**:711–728, 2006.

[82] J. F. Morris and F. Boulay. Curvilinear flows of noncolloidal suspensions: The role of normal stresses. *J. Rheol.*, **43**:1213–1237, 1999.

[83] D. Lhuillier. Migration of rigid particles in non-brownian viscous suspensions. *Phys. Fluids*, **21**(2):023302, 2009.

[84] P. R. Nott, E. Guazzelli, and O. Pouliquen. The suspension balance model revisited. *Phys. Fluids*, **23**:043304, 2011.

[85] A. Franceschini, E. Filippidi, E. Guazzelli, and D. J. Pine. Transverse alignment of fibers in a periodically sheared suspension: An absorbing phase transition with a slowly varying control parameter. *Phys. Rev. Lett.*, **107**:250603, 2011.

[86] J. M. Bricker and J. E. Butler. Correlation between structures and microstructures in concentrated suspensions of non-Brownian spherical particles subject to unsteady shear flows. *J. Rheol.*, **51**:735–759, 2007.

[87] O. L. Forgacs and S. G. Mason. Particle motions in sheared suspensions: *IX*. Spin and deformation of threadlike particles. *J. Colloid Sci.*, **14**(5):457–472, 1959.

[88] L. H. Switzer and D. J. Klingenberg. Rheology of sheared flexible fiber suspensions via fiber-level simulations. *J. Rheol.*, **47**(3):759–778, 2003.

[89] E. Lauga. Floppy swimming: Viscous locomotion of actuated elastica. *Phys. Rev. E*, **75**:041916, Apr 2007.

[90] E. Wandersman, N. Quennouz, M. Fermigier, A. Lindner, and O. Du Roure. Buckled in translation. *Soft Matter*, **6**:5715, 2010.

[91] C. H. Wiggins and R. E. Goldstein. Flexive and propulsive dynamics of elastica at low Reynolds number. *Phys. Rev. Lett.*, **80**:3879–3882, 1998.

[92] Y. N. Young and M. J. Shelley. Stretch-coil transition and transport of fibers in cellular flows. *Phys. Rev. Lett.*, **99**(5):058303, 2007.

[93] S. Bounoua, P. Kuzhir, and É. Lemaire. Normal stress differences in non-Brownian fiber suspensions. *J. Rheol.*, **60**(4):661–671, 2016.

[94] F. da Cruz, S. Emam, M. Prochnow, J. Roux, and F. Chevoir. Rheophysics of dense granular materials: Discrete simulation of plane shear flows. *Phys. Rev. E*, **72**:021309, 2005.

[95] P. Jop, Y. Forterre, and O. Pouliquen. A constitutive law for dense granular flows. *Nature*, **441**(7094):727–730, 06 2006.

[96] Y. Forterre and O. Pouliquen. Flows of dense granular media. *Ann. Rev. Fluid Mech.*, **40**(1):1–24, 2008.

[97] J. J. Stickel and R. L. Powell. Fluid mechanics and rheology of dense suspensions. *Annu. Rev. Fluid Mech.*, **37**:129–149, 2005.

## BIOGRAPHICAL SKETCH

Saif Shaikh was born in Mumbai, India. His mother was a pre-school teacher and his father was a laboratory technician for an institute of cardiology in Pune, India. He attended St. Vincent's High School for his elementary, middle, and high school where he played basketball and was part of the boy scout movement.

Saif attended the University of Pune, where he received a Bachelor of Engineering degree, majoring in Chemical Engineering. His favorite courses at the University of Pune were fluid mechanics, and engineering materials. He pursed a research internship at the National Chemical Laboratory in Pune, India under the supervision of Dr. Sanjeev Tambe after his undergraduate studies.

Upon the completion of his internship, Saif was admitted to the graduate program at the University of Florida where he obtained a Master of Science degree, majoring in Chemical Engineering. He participated in a research program under Dr. Jason E. Butler which led him to be accepted to the PhD program upon graduation.

He continued his education at the University of Florida in chemical engineering and Aix-Marseille University in physics of fluids. He was co-advised by Dr. Jason E. Butler at the University of Florida and Dr. Élisabeth Guazzelli at Aix-Marseille University. He carried out experimental work at Aix-Marseille University and performed data analyses at the University of Florida. He received a dual PhD in these disciplines in 2017 and is looking forward to continuing work in fluid mechanics and rheology in the pharmaceutical or manufacturing industry.